ISSN 2435-5453

Technical Journal of Advanced Mobility

次世代移動体技術誌

巻 頭 言

論 文

JUADA
Japan UAS Industrial Development Association

Vol. 7
2026

フィジカル AI ドローンのジャーナル

テクニカルジャーナル編集委員長
一般社団法人日本 UAS 産業振興協議会
常務理事　岩田　拡也

2026 年が幕を開けました。謹んで新年のご挨拶を申し上げます。

一般社団法人日本UAS産業振興協議会(JUIDA)が発行するTechnical Journal of Advanced Mobility(TJAM)は、ドローン産業の振興に役立つ技術情報を産業界の皆様に提供するために創設されたオンライン技術情報誌で、掲載論文は年々増加を続けております。毎年進化を続ける TJAM ですが、昨年 2025 年も例えば、Letter で一度発表した後、正式に論文で再投稿されるパターンや、英語版と日本版（母国語版）の両方掲載できる新しい制度を活用する著者も出て参りました。今後は世界のドローンおよびエアモビリティ関係者に読んで頂けるジャーナルを目指して参ります。その一環として 2026 年から巻頭言も英語版をご用意することとなりました。今後とも TJAM をグローバルに活用して頂ければ幸いです。

そのグローバルの話題ですが、毎年多くの国々の参加で活況を呈している Japan Drone 展で、2026 年もポスターセッション開催が決定しております。今年もプレゼンコーナーをご用意しておりますので、若手研究者や学生の在籍する研究室からのご参加をお待ちしております。また Japan Drone のポスターセッションは、学術論文でオーサービジットが可能な貴重な機会ですので、今年も著者に集まっていただけるような場を検討しております。本ジャーナルの著者は産業界や学術界など多岐に渡る分野の方々ですので、産官学一体となって情報交換や情報共有を促進するエコシステムの役割も TJAM は果たします。この役割は国境を越えてグローバルに存在しますので、海外からの投稿も積極的に募集していきたいと考えております。

今年 2026 年は、世界が大きく変革する節目と目されていて、FAA のパート 108 の高度に自動化した目視外飛行など先進的な空の技術と向き合いチャレンジするまさに「天馬行空」の年です。下水管内を点検するマイクロドローンから、数千機同時飛行するドローンショー、成層圏に浮かぶ巨大な HAPS 型宇宙光通信６Ｇドローンまで、無人航空機やエアモビリティの技術は多様化しています。TJAM は、その多様な新技術の発展と情報共有に貢献して参ります。本年も何卒宜しくお願い申し上げます。

2026 年 1 月吉日

岩田　拡也 Kakuya Iwata

国立研究開発法人 産業技術総合研究所上級主任研究員。1998 年通商産業省工業技術院 電子技術総合研究所に入所。第 16 回電子材料シンポジウム EMS 賞受賞。第 12 回応用物理学会講演奨励賞受賞。青色 LED 開発、半導体製造装置開発から産業用飛行ロボット開発に至り、2007 年日本機械学会交通・物流部門優秀講演表彰を受賞。2008 年に経済産業省 製造産業局 産業機械課にてロボット政策に従事。2009 年以降「NIIGATA SKY PROJECT」の無人航空機開発を立ち上げ、2014 年に JUIDA 設立。2018 年より ISO TC 20/SC 16(無人航空機)に参加し、2022 年経済産業省 産業標準化事業表彰受賞、日本品質管理学会第 52 回年次大会研究発表会優秀発表賞受賞。

Foreword: 'The Journal for Physical AI Drones'

Chairman of the Technical Journal Editorial Committee
Japan UAS Industrial Development Association (JUIDA)
Executive Director Kakuya Iwata

The year 2026 has commenced. We extend our sincere New Year's greetings.
The Technical Journal of Advanced Mobility (TJAM), published by the Japan UAS Industrial Development Association (JUIDA), is an online technical information magazine established to provide industry stakeholders with technical information beneficial to the advancement of the drone industry. The number of papers published continues to increase year by year. While the Technical Journal continues to evolve annually, last year (2025) saw new patterns emerge. For instance, authors first published a Letter before formally resubmitting it into a full paper, and some utilized the new system allowing simultaneous publication in both English and Japanese (native language) editions. Moving forward, we aim to develop the journal into one accessible to drone and air mobility professionals worldwide. As part of this effort, from 2026, the opening statement will also be available in English. We would be delighted if TJAM continues to be utilized by readers around the world.
Regarding global engagement, the poster session at Japan Drone, which sees lively participation from many countries each year, has been scheduled for 2026. We will again provide a presentation corner and look forward to participation from laboratories with young researchers and students. Furthermore, the Japan Drone poster session offers a valuable opportunity for author visits based on academic papers, so we are considering ways to encourage authors to gather there again this year. As authors of this journal span diverse fields including industry and academia, TJAM also serves as an ecosystem promoting information exchange and sharing across industry, government, and academia. This role extends globally beyond national borders, so we actively encourage submissions from overseas.

The year 2026 is viewed as a pivotal moment of significant global transformation. It is truly a year of boundless imagination, confronting and challenging advanced aerial technologies such as the highly automated beyond visual line of sight (BVLOS) flights under FAA Part 108 regulations. From micro-drones inspecting sewer pipes to drone shows involving thousands flying simultaneously, and even massive HAPS-type space optical communication 6G drones floating in the stratosphere, unmanned aerial vehicle and air mobility technologies are diversifying. TJAM will contribute to the development and information sharing of these diverse new technologies. We look forward to your continued support this year.

January 2026

Kakuya Iwata

Senior Principal Researcher, National Institute of Advanced Industrial Science and Technology (AIST). Joined the Electronics and Telecommunications Research Institute, Agency of Industrial Science and Technology, Ministry of International Trade and Industry (MITI) in 1998. Recipient of the 16th Electronic Materials Symposium EMS Award. Recipient of the 12th Applied Physics Society Presentation Encouragement Award. His work spans from blue LED development and semiconductor production equipment development to industrial flying robot development. Received the 2007 Japan Society of Mechanical Engineers Transportation and Logistics Division Outstanding Presentation Award. Engaged in robot policy at the Industrial Machinery Division, Manufacturing Industries Bureau, Ministry of Economy, Trade and Industry in 2008. Launched the unmanned aircraft development for the "NIIGATA SKY PROJECT" in 2009, establishing JUIDA in 2014. Served as an ISO TC20/SC16 (Unmanned Aircraft Systems) expert since 2018. Received the Ministry of Economy, Trade and Industry Industrial Standardization Project Award in 2022 and the Excellent Presentation Award at the 52nd Annual Conference Research Presentation Session of the Japan Society for Quality Control in 2022.

Development of CO_2 Gas Sensing Method using Formation Flight with Four Drones

Shanfeng Zhang[*1], Shigenori Togashi[*2], Etsuki Yoshimura[*2]
Graduate School of Advanced Science and Engineering, Waseda University[*1]
Mechanical Engineering Course, School of Science and Engineering, Kokushikan University[*2]

Understanding gas concentration distributions near the ground is important for disaster prevention and safety management. In this study, as part of expanding drone applications, we tried to develop the CO_2 gas sensing method using formation flight with four drones. By flow simulation, we confirmed the gas updraft flow not only velocity but also concentration distribution generated by the drones. It was confirmed that the updraft flow velocity around the sensor was 2 m/s at the height of 0.3 m, and the concentration ratio was between 0.95 and 0.99, respectively. Then, to stable the formation flight with four drones, a rope was used between the connecting rod and the drone. Then, the CO_2 sensing experiment using this approach was conducted. The average concentration values of 4,290 and 4,710 ppm of three experiments were measured at the heights of 0.5 m and 0.3 m, respectively. Moreover, we tried to predict the concentration at the CO_2 source using the steady-state one-dimensional convection-diffusion equation. It was found that the predicted concentration of 4,772 ppm at the CO_2 source was in between 4,700 and 4,800 ppm measured by sensor. Finally, the effectiveness of prediction was confirmed.

Keywords: Drone, Formation flight, Flow simulation, Gas sensing, Convection, Diffusion, Prediction

1. Introduction

There is a wide range of possible applications for drones, such as for infrastructure inspection, agriculture, logistics, photography, disaster prevention, and gas sensing. In dangerous site inspection, their ability to quickly collect information in hazardous areas where human entry is dangerous has become increasingly important. The poisonous hydrogen sulfide (H_2S) gas and high concentration CO_2 gas, being heavier than air, tend to accumulate near the ground in underground or enclosed spaces, potentially causing delayed responses, oxygen deficiency, or poisoning. Understanding gas concentration distributions in such environments is important for disaster prevention and safety management. In recent years, papers have been published on the use of drones for gas sensing tasks. Li, et al. [1] reported the air quality monitoring, and Motlagh, et al. [2] reported the air pollution monitoring using a drone in flight, respectively. On the other hand, Neumann, et al. [3] reported results of gas source localization experiments using a drone equipped with several different types of gas sensors by applying a particle filter-based algorithm to the sensor data collected in flight. Successful gas source localization demonstrations were also reported for a drone equipped with a laser-based remote methane detector [4]. Despite these successful examples, there is a problem using drone for gas sensing tasks. The rotors of a drone produce a strong downwash to obtain the lift force. Most gas sensors show a response only when a gaseous chemical substance touches the sensor surface. The gas contained in the surrounding air needs to be transported to the sensor surface by convection and diffusion. When a drone flies, the downwash generated by rotors blows off the gas near the ground. This problem has been raised even in early work on gas sensing drones [5]. To solve the above problem, Sato, et al. [6] proposed the gas sensing method by using the fountain flow [7]

generated by the two drones connected by a rod. In their paper, the flow velocity distribution by numerical simulation and the experimental results with air were also reported. Moreover, Akaogi, et al. [8] proposed the gas sensing method by using the fountain flow generated by the extended arm quad type drone. In their paper, their experimental results with ethanol gas were also reported.

In the above previous studies, there are still some issues as follows. First, the gas updraft flow velocity distribution generated by the drones is shown using flow simulation, but the gas concentration distribution is not shown. Second, the formation flight equipped with the gas sensor is unstable in case of direct connection between rods and each drone. Third, there was no prediction of CO_2 concentration at the source based on the sensing point.

Therefore, in this study, we assumed the application example of CO_2 sensing with heavier than air and larger amount at the underground parking lot as shown in **Fig.1**. First, flow simulation was conducted to visualize the gas updraft flow not only flow velocity but also concentration distribution generated by the drones as detailed in Chapter 2. Second, the formation flight equipped with the gas sensor is unstable in case of direct connection between rods and each drone. Therefore, a rope was used between the connecting rod and the drone, instead of connecting the rod directly to the drone. With this approach, the individual differences of drone position and height were compensated for by the rope, and the formation flight with four drones were stably continued as detailed in Chapters 3 and 4. Third, we conducted CO_2 sensing experiments using formation flight with four drones and predicted CO_2 concentration at the source from the sensing points using the one-dimensional convection-diffusion equation as detailed in Chapters 5, 6, and 7.

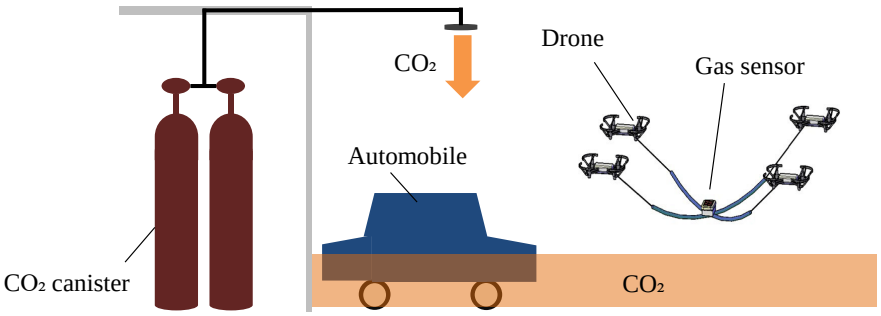

Fig.1 Application example of CO_2 sensing at the underground parking lot.

2. Flow simulation

To visualize the gas updraft flow not only flow velocity but also concentration distribution generated with the drones, flow simulation was conducted using the software Flowsquare$^+$ [9-11]. The gas concentration transport equation is also solved with the momentum transport equation in Flowsquare$^+$, and the application example papers have been published [12,13]. **Figure 2** shows the flow simulation domain and boundary conditions of flow simulation around two drones. Parameters lx, ly, lz, nx, ny, and nz represent Length in x, y, z direction, number of grids in x, y, and z direction, respectively. **Table 1** is specification of parameters using the boundary conditions of flow simulation. Here, the domain in the z direction was thinned to perform quasi-two-dimensional simulation. Parameters W_d, P_d, and H_d represent the width of drone, the diameter of drone propeller, and hovering height, respectively. Flow simulation conducted both one drone and two drones. In case of two drones, L represents the distance between drones as shown in **Fig.2**. Parameters VinG and VinR are the inflow velocity at the top of drone propeller (Boundary color: Green) and the outflow velocity at the bottom of drone propeller (Boundary color: Red) measured with a Pitot tube and set to 8 m/s as the velocity boundary condition of drone

1. Similar boundary conditions were also set for drone 2. Parameters W_s, H_s, and D_s represent the width of sensor housing, installation height of sensor housing, and thickness of sensor housing, respectively. Here, the sensor housing was set only in case of simulation for two drones.

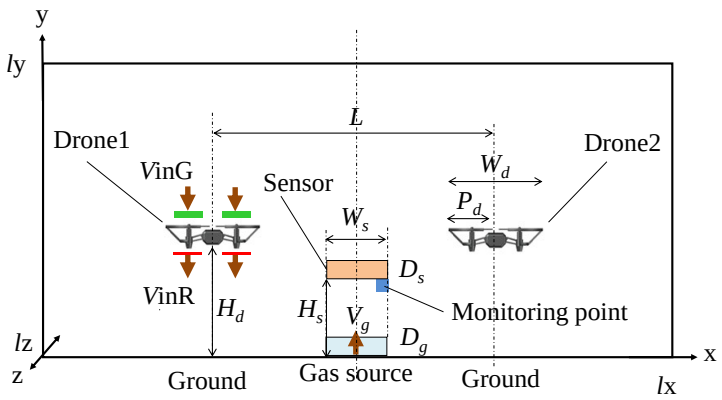

Fig.2 Flow simulation domain and boundary conditions.

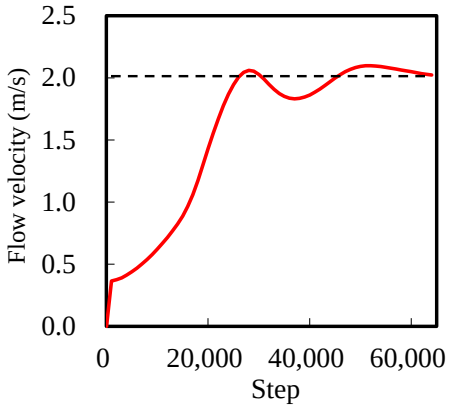

Fig.3 Flow velocity convergence at the monitoring point.

Table 1 Specification of parameters using the boundary conditions of flow simulation.

No.	Parameters	Explanation of parameters	Input data	
			One drone	Two drones
1	*lx*	Length in x direction (m)	2.5	2.5
2	*ly*	Length in y direction (m)	1.0	1.0
3	*lz*	Length in z direction (m)	0.05	0.05
4	*nx*	Number of grids in x direction	250	250
5	*ny*	Number of grids in y direction	100	100
6	*nz*	Number of grids in z direction	5	5
7	W_d	Width of drone (m)	0.20	0.20
8	P_d	Diameter of drone propeller (m)	0.08	0.08
9	H_d	Hovering height (m)	0.4	0.4
10	L	Distance between drones (m)	-	1.5
11	*V*inG	Inflow velocity at the top of drone propeller (Boundary color: Green)	-8.0	-8.0
12	*V*inR	Outflow velocity at the bottom of drone propeller (Boundary color: Red)	-8.0	-8.0
13	W_s	Width of sensor housing (m)	-	0.2
14	H_s	Installation height of sensor housing (m)	-	0.3
15	D_s	Thickness of sensor housing (m)	-	0.05
16	D_g	Thickness of gas ejection source (m)	-	0.05
17	V_g	Gas ejection velocity (m/s)	0.1	0.1
18	C_g	Gas concentration ratio	1.0	1.0
19	*mu*	Air viscosity coefficient (Pa·s)	1.8×10^{-5}	1.8×10^{-5}
20	C_s	Coefficient of Smagorinsky turbulence model	0.17	0.17
21	*cfl*	Courant-Friedrichs-Lewy number	0.01	0.01

Parameters D_g, V_g, and C_g represent the thickness of gas ejection source, gas ejection velocity, and gas concentration ratio, respectively. Last parameters *mu*, C_s, and *cfl* represent air viscosity coefficient, the coefficient of Smagorinsky turbulence model [14,15], and Courant-Friedrichs-Lewy number, respectively. For stable flow simulation, the Courant number (CFL) number for the explicit method was set to a small value of 0.01. **Figure 3** shows the state of flow velocity convergence at the monitoring point near the sensor in **Fig.2**. It was confirmed that the flow velocity at the monitoring point converged to approximately 2.0 m/s after 63,000 simulation steps.

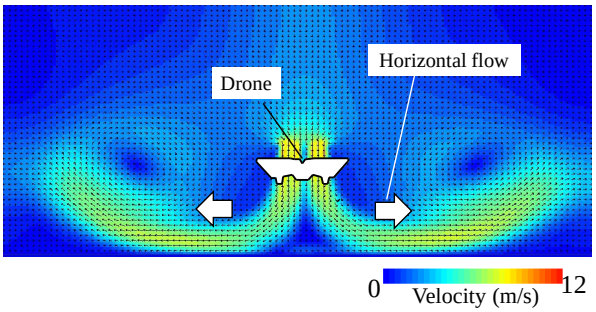

(a) Flow velocity distribution

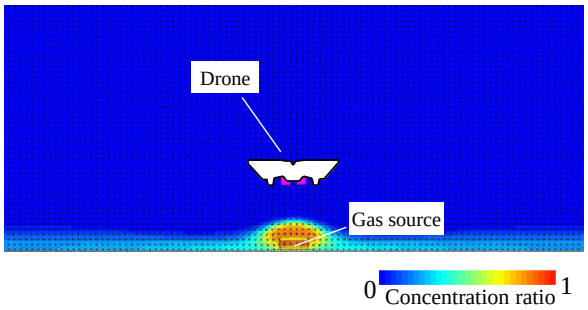

(b) Concentration distribution

Fig.4 Flow simulation results in case of one drone.

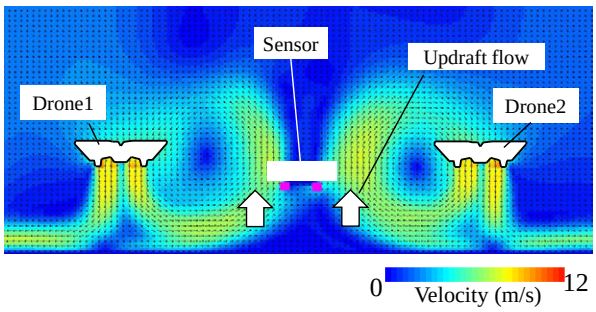

(a) Flow velocity distribution

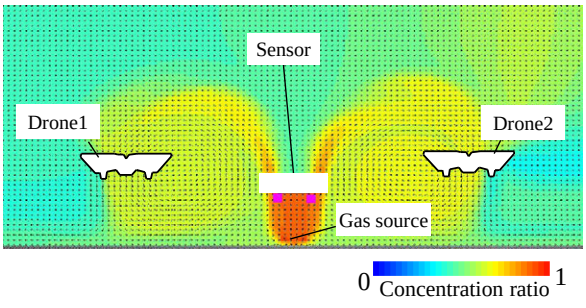

(b) Concentration distribution

Fig.5 Flow simulation results in case of two drones.

Figure 4 shows the flow simulation results in case of one drone. **Figures 4(a)** and **4(b)** are the flow velocity and concentration distribution, respectively. The downwash flow generated by the drone spread out as the horizontal flow along the ground after reaching the ground as shown in **Fig.4(a)**. Therefore, it has been confirmed that the concentration distribution from the gas source became horizontally as shown in **Fig.4(b)**. Here, the concentration distribution is expressed as the normalized concentration ratio and ranges from 0 to 1.

Figure 5 shows the flow simulation results in case of two drones. **Figures 5(a)** and **5(b)** are the flow velocity and concentration distribution, respectively. The downwash flow generated by two drones rolled up as the updraft flow after reaching the ground. Therefore, it has been confirmed that the concentration from the gas source became updraft flow and reached the sensor shown in **Fig.5(b)**. Moreover, it was confirmed that the concentration ratio around the sensor was between 0.95 and 0.99.

3. CO_2 gas sensor

For the formation flight with four drones, the requirements of CO_2 gas sensor are lightweight (100 g or less) and wireless communication function. As a sensor with satisfying the above requirements, we selected the RICOH EH CO_2 sensor D101 [16] as shown in **Fig.6**. **Figures 6(a)** and **6(b)** show the surface side with wireless communication using the solar panel and the protective housing, and reverse side with four intake ports (No.1-4) and two exhaust ports (No.5,6). **Figure 6(c)** shows the inner configuration using NDIR (Non Dispersive IfraRed)-type. The CO_2 concentration was calculated from Eq. (1).

$$T = \frac{I}{I_0} = e^{-\varepsilon C d} \tag{1}$$

where T, I, I_0, ε, C, and d represent transmittance, intensity of transmitted light, intensity of incident light, absorbance, CO_2 concentration, and optical path length, respectively.

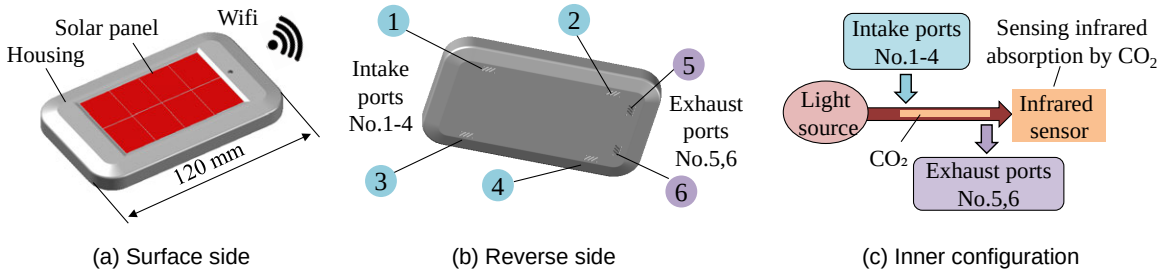

Fig.6　Schematic of CO_2 sensor module and inner configuration.

4. Design of formation flight configuration

Figure 7 shows a schematic of formation flight configuration with four drones and the control method. The drone used was a Tello EDU with specifications listed in Table 2. The four drones were simultaneously controlled by a single personal computer using Python program. A rope was used between the connecting rod and the drone with a spacing of 1.3 m, instead of connecting the rod directly to the drone [17,18] as shown in Fig.7. With this approach, the individual differences of drone position and height were compensated for by the rope, and the formation flight with four drones were stably continued. The CO_2 sensor was suspended at the center of a four-drone square formation and the concentration data were sampled at 10 second intervals in the tablet computer by wireless communication function.as shown in Fig.7. The payload of a Tello EUD is 30 g as shown in Table 2. Therefore, the total payload of the formation flight with four drones becomes 120 g, and the total components weight was 111 g less than the required 120 g with the weight breakdown of components listed in Table 3.

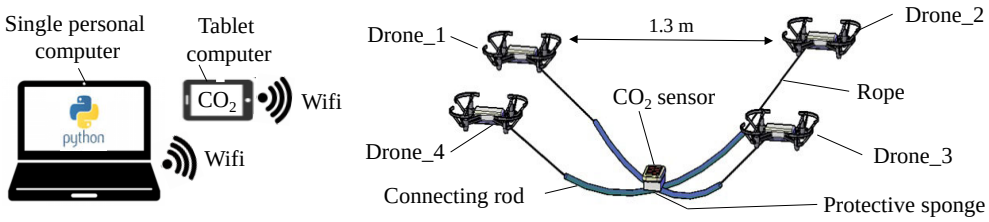

Fig.7　Schematic of formation flight configuration with four drones and the control method.

Table 2　Specifications of a drone.

Drone	Tello EDU
Payload of a drone (g)	30
Weight (g)	87
Maximum flight time (min)	13
Number of formation flights	4

Table 3　Weight breakdown of components.

Component	Number	Weight [g]
Connecting rod	4	16
Protective sponge	1	1
CO_2 sensor	1	90
Rope	4	4
Total weight (g)	-	111 < 120

5. CO_2 gas sensing experiment at the fixed position

Figure 8 shows a schematic of CO_2 sensing experiment at the fixed position. The CO_2 gas was generated by placing 400 g of dry ice in 300 g of water (mass ratio 4:3) into a plastic container with the size of 220 × 170 × 50 mm as the CO_2 gas source. The CO_2 gas source concentration was measured to be between 2,200 and 2,300 ppm by sensor. The four-drone formation hovered so that the height of CO_2 sensor kept 0.3 m, and the plastic container of CO_2 gas source was in at 5 seconds and out at 90 seconds under the four-drone formation as shown in Fig.8.

The initial indoor concentration was approximately 1,000 ppm. **Figure 9** shows the sensing results of CO_2 concentration for 160 seconds. When the four-drone formation was fixed in hovering mode directly above the dry ice source at a height of 0.3 m. In 5 seconds, the plastic container of CO_2 gas source was in under the four-drone formation. In 55 seconds, the maximum concentration of 2,100 ppm was observed corresponding to an increase of approximately 1,100 ppm over the background concentration. Moreover, in 90 seconds, the plastic container of CO_2 gas source was out, and in 160 seconds, CO_2 concentration returned to initial value as shown in **Fig.9**.

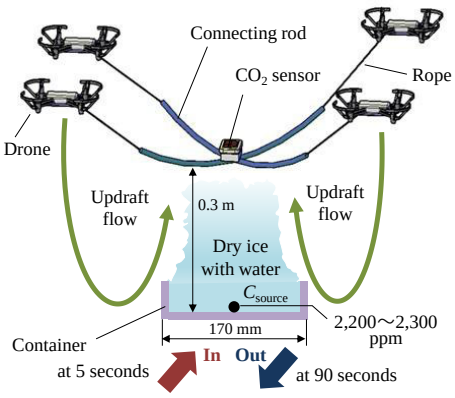

Fig.8 Schematic of CO_2 sensing experiment at the fixed position.

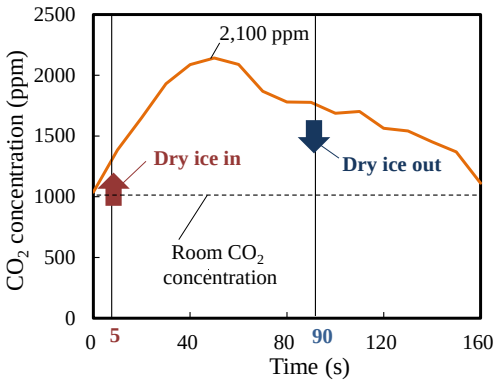

Fig.9 Sensing results of CO_2 concentration.

6. CO_2 gas sensing experiment with the horizontal flight

Figure 10 shows a schematic of CO_2 sensing experiment with the horizontal flight. The CO_2 gas was generated by placing 1,600 g of dry ice in 1,200 g of water (mass ratio 4:3) into four plastic containers with the size of $220 \times 170 \times 50$ mm as the CO_2 gas source. The CO_2 gas source concentration was measured to be between 4,700 and 4,800 ppm by sensor as shown in **Fig.10**.

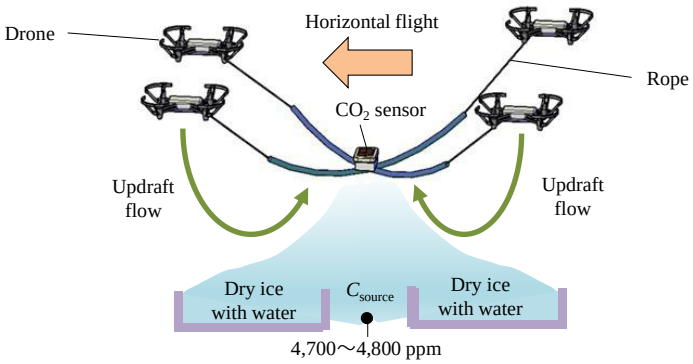

Fig.10 Schematic of experiment with the horizontal flight.

The experiment was conducted three times, and the amount of dry ice decreased over time. Therefore, dry ice was added as needed to ensure the concentration was within the range of 4,700 to 4,800 ppm before the experiment was conducted. Additionally, experiments were conducted at two heights of 0.3 m and 0.5 m. By using Python-based automatic flight control, a flight sequence consisting of takeoff, horizontal movement, hovering for 10 seconds above the CO_2 source, retreat, and landing. The influence of horizontal movement on

the updraft flow behavior of the formation was evaluated.

Figure 11 shows photographs of CO_2 sensing experiment with the horizontal flight. **Figure 11(a)** shows flight at the height of 0.5 m, and **Figure 11(b)** shows flight at the height of 0.3 m. **Figure 12** shows sensing results of the CO_2 concentration **Figure 12(a)** shows the CO_2 concentration at the height of 0.5 m, and it was confirmed that the concentration increased to a maximum of 4,230 ppm. **Figure 12(b)** shows the CO_2 concentration at the height of 0.3 m, and it was confirmed that the concentration increased to a maximum of 4,673 ppm. Additionally, the prediction of CO_2 concentration at the source based on the two sensing points is conducted in next Chapter 7.

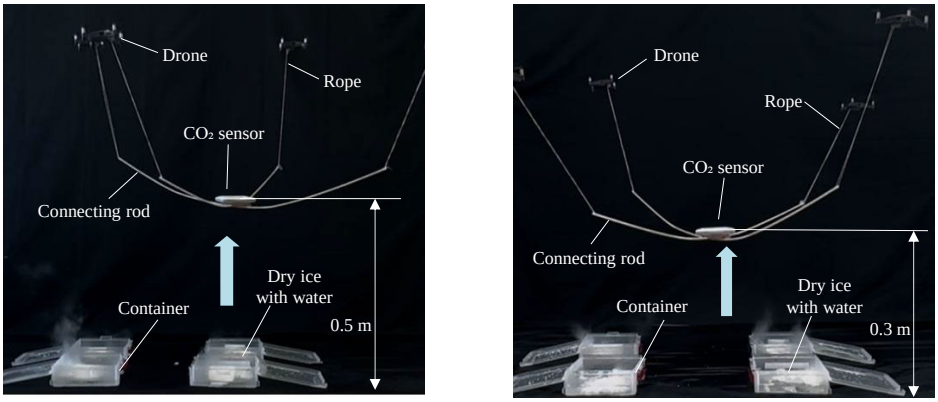

(a) Flight at the height of 0.5 m　　(b) Flight at the height of 0.3 m

Fig.11 Photographs of CO_2 sensing experiment with the horizontal flight at the hovering for 10 seconds.

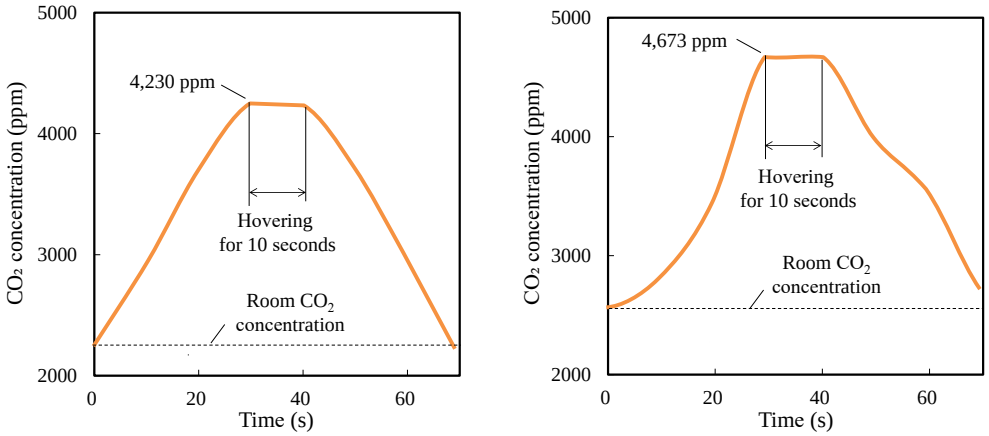

(a) Flight at the height of 0.5 m　　(b) Flight at the height of 0.3 m

Fig.12 Sensing results of CO_2 concentration.

7. Prediction of CO_2 concentration at the source

To predict CO_2 concentration at the source based on the two sensing points at the heights of 0.5 m and 0.3 m, the steady-state one-dimensional convection-diffusion equation [19] is used as shown in Eq. (2).

$$u\frac{dC}{dz} = D_t\frac{d^2C}{dz^2} \tag{2}$$

where C, u, z, and D_t represent concentration, velocity, vertical coordinates, and turbulent diffusion coefficient, respectively. Equation (2) has the exact solution with the boundary condition: $C = C_0$ at $z = 0$, $C = C_H$ at $z = H$ as

shown in Eq. (3).

$$C(z) = C_0 + \frac{e^{Pe\frac{z}{H}} - 1}{e^{Pe} - 1}(C_H - C_0) \tag{3}$$

Here, Pe is Peclet number defined as Eq. (4) using turbulent diffusion coefficient D_t.

$$Pe = \frac{uH}{D_t} \tag{4}$$

Table 4 shows the values for calculation of Peclet number Pe, we used CO_2 molecular diffusion coefficient $D_m = 1.64 \times 10^{-5}$ m^2/s [20], and ratio of turbulent to molecular diffusion coefficient $D_t / D_m = 10^4$ (Average of 10^3–10^5) [21].

Table 4 Values for calculation of Peclet number Pe.

CO_2 molecular diffusion coefficient [20] D_m (m^2/s)	Ratio of turbulent to molecular diffusion coefficient [21] D_t / D_m	Velocity u (m/s)	Height H (m)
1.64×10^{-5}	10^4 (Average of $10^3 - 10^5$)	2.0	0.5

Table 5 shows the predicted result of concentration at the CO_2 source. The average concentration values of 4,290 and 4,710 ppm of three experiments ($N = 3$) were used at the heights of 0.5 m and 0.3 m, respectively. By substituting these average concentrations into Eqs. (3) and (4), the concentration at the CO_2 source was predicted as 4,772 ppm. Additionally, it was found that the predicted concentration of 4,772 ppm at the CO_2 source was in between 4,700 and 4,800 ppm measured by sensor as shown in Fig.12. Finally, the effectiveness of prediction was confirmed.

Table 5 Predicted result of concentration at the CO_2 source in case of horizontal fight experiment (Fig.12).

Height (m)	Concentration (ppm)	Method
0.5	4,290	Experimental average $N = 3$
0.3	4,710	Experimental average $N = 3$
0.0 (CO_2 source)	4,772	Using Eqs. (3) and (4)

8. Discussion

It is necessary for gas sensing using drones to consider the drone down's wash flow. Therefore, there are four categories based on the amount of gas generation and the specific gravity relative to air. First category is the gas lighter than air and small amount. Second category is the gas lighter than air and large amount. Third category is the gas heavier than air and small amount. Fourth category is the gas heavier than air and large amount. Here, the determination whether to the large or small amount is based on the following criteria, that is, the large amount is defined as that the stable gas supply is larger than the blowing away by the drone's downwash.

This study belongs to fourth category, and we need to generate the updraft flow for sensing the gas heavier than air and large amount. In contrast, in case of first and third categories, the sensor must be suspended using a sufficiently long rope to avoid the influence of the flying drone's downwash. Additionally, in case of second category, the regular drone equipped with sensor can land on the gas source and sense the gas because the gas

is lighter than air and large amount. To conduct the study in the above categories, it is necessary to solve the distance reached by the drone's downwash using flow simulation. We have already conducted the above study and plan to report in next paper.

9. Conclusion

In this study, as part of expanding drone applications, we tried to develop the CO_2 gas sensing method using formation flight with four drones. Flow simulation of the gas updraft flow, the construction of formation flight, CO_2 sensing experiments, and prediction of CO_2 concentration at the source were conducted. The following conclusions were obtained.

(1) By flow simulation, we confirmed the gas updraft flow not only velocity but also concentration distribution generated by the drones. It was confirmed that the updraft flow velocity around the sensor was 2 m/s at the height of 0.3 m, and the concentration ratio was between 0.95 and 0.99, respectively.
(2) A rope was used between the connecting rod and the drone, instead of connecting the rod directly to the drone. With this approach, the individual differences of drone position and height were compensated for by the rope, and the formation flight with four drones were stably continued. Then, the CO_2 sensing experiment using this approach was conducted. The average concentration values of 4,290 and 4,710 ppm of three experiments were measured at the heights of 0.5 m and 0.3 m, respectively.
(3) Moreover, prediction of the concentration at the CO_2 source was conducted using the steady-state one-dimensional convection-diffusion equation. It was found that the predicted concentration of 4,772 ppm at the CO_2 source was in between 4,700 and 4,800 ppm measured by sensor. Finally, the effectiveness of prediction was confirmed.

Received: December 8, 2025
Accepted: January 7, 2026

References

[1] Li, Y., Huang, Y. and Chen, S.: "Air Quality Detection Drone System Based on Beidou Navigation System," *Computer Science and Application*, Vol. 9, No. 4, Article ID: 29659, pp. 703–709, 2019.
[2] Motlagh, N.H., Kortoçi, P., Su, X. and Lovén, L.: "Unmanned Aerial Vehicles for Air Pollution Monitoring: A Survey," *IEEE Internet of Things Journal*, Vol. 10, No. 24, pp. 21687–21704, 2023.
[3] Neumann, P.P., Hernandez Bennetts, V., Lilienthal, A.J., Bartholmai, M. and Schiller, J.H.: "Gas source localization with a micro-drone using bio-inspired and particle filter-based algorithms," *Adv. Robot.*, Vol. 27, pp. 725–738, 2012.
[4] Golston, L.M., Aubut, N.F., Frish, M.B., Yang, S., Talbot, R.W., Gretencord, C., McSpiritt, J. and Zondlo, M.A.: "Natural gas fugitive leak detection using an unmanned aerial vehicle: Localization and quantification of emission rate," *Atmosphere*, Vol. 9, No. 333. pp. 1–17, 2018.
[5] Neumann, P.P., Asadi, S., Lilienthal, A.J., Bartholmai, M. and Schiller, J.H.: "Autonomous gas-sensitive microdrone: Wind vector estimation and gas distribution mapping," *IEEE Robot. Autom. Mag.*, Vol. 19, pp. 50–61, 2012.
[6] Sato, R., Tanaka, K., Ishida, H., Koguchi, S., Ramirez., J. P. R., Matsukura, H. and Ishida, H.: "Detection of Gas Drifting Near the Ground by Drone Hovering Over: Using Airflow Generated by Two Connected Quadcopters," *Sensors*, Vol. 20, No. 5, pp. 1–16, 2020.
[7] Li, Q., Page, G.J. and McGuirk, J.J.: "Large-eddy simulation of twin impinging jets in cross-flow," *Aeronaut. J.* Vol. 111, pp.195–206, 2007.
[8] Akaogi, D., Yamashita, K., Matsukura, H., and Ishida, H.: "Development of Gas Sensing Drone: Influence of Tilted Ground on

Gas Transport," *Proc. of The Japan Society of Mechanical Engineers*, S115-05, 2021.
[9] Minamoto, Y.: "Numerical Thermo-Fluid Dynamics with Fluid Simulation Software Course Flowsquare$^+$(1)," *Journal of Mechanical Research*, Vol. 72, No. 9, pp. 677–681, 2020.
[10] Trájer, A. J.: "Ecological evaluation of the development of Neanderthal niche exploitation," *Quaternary Science Reviews*, Vol. 310, 108127, 2023.
[11] Tajima, Y., Hiraguri, T., Matsuda, T., Imai, T., Hirokawa, J., Shimizu, H., Kimura, T. and Maruta, K.: "Analysis of Wind Effect on Drone Relay Communications," *Drones* Vol. 7, No. 3, 182, https://doi.org/10.3390/drones7030182, 2023.
[12] Togashi, S., Zhang, H. and Miyake, R.: "Development of a measuring system for the volatilization characteristics of essential oils and evaluation of the measured data by advection–diffusion simulation," *Japan Journal of Aromatherapy*, Vol. 26, No. 1, pp. 1–9, 2025.
[13] Ishigaki, Y., Kawauchi, Y., Yokogawa, S., Saito, A., Kitamura, H. and Moritake, T.: "Ventilatory effects of excessive plastic sheeting on the formation of SARS-Cov-2 in a closed indoor environment," *Environmental and Occupational Health Practice*, 5: eohp.2022-0024-OA, pp. 1–9, 2023.
[14] Koyama, S.: "Large eddy simulation of the turbulent pipe flow using dynamic subgrid-scale model," *Institute of Industrial Science*, Vol. 57, No. 1, pp. 58–62, 2005.
[15] Fujiwara, S.: "Experimental Study on Synchronized Swimming in the Kármán Vortex Behind an Object Using a Fish Robot," *Journal of Aero Aqua Bio-mechanisms*, Vol. 11, No. 1, pp. 10–17, 2025.
[16] Takeuchi, K.: "Current status and future of energy harvesting technologies," *Journal of the Japan Society for Precision Engineering*, Vol. 88, No. 11, pp. 805–808, 2022.
[17] Ando, T. and Togashi, S.: "Flight Stability Analysis of Formation Drones and Application to Netting Operation," *Technical Journal of Advanced Mobility*, Vol. 6, No. 8, pp. 57–66, 2025.
[18] Ando, T., Aoki, H. and Togashi, S.: "Flight Stabilization of Drones near Ceiling and Its Application to Cabling," *Proc. of the 30th Annual Meeting of Kanto Branch*, JSME, 14G02, 2024.
[19] Ferziger, J. and Peric, M.: Computational method for fluid dynamics, 3rd Edition, Springer, pp. 76–83, 2002.
[20] Matsunaga, N., Hori, M. and Nagashima, A.: "5th Report Measurements of the mutual diffusion coefficients of gases by the Taylor method," *Transactions of the Japan Society of Mechanical Engineers.* Part B, Vol. 64; No. 621, pp. 149–155, 1998.
[21] Levenspiel, O.: Chemical Reaction Engineering, 3rd ed., John Wiley & Suns, p. 311, 1999.

張　山峰
2025 年 3 月国士舘大学理工学部機械工学系卒業。富樫研究室に所属時に編隊飛行する 4 台のドローンによる CO_2 検知法を開発し，Technical Journal of Advanced Mobility ポスターセッション in Japan Drone 2025 に発表。2025 年 4 月早稲田大学大学院生命理工専攻に進学。現在，介護分野へのセンシング技術の応用拡大に取り組んでいる。
E-mail：zsf@akane.waseda.ac.jp

吉村　越輝
2022 年 4 月 国士舘大学理工学部機械工学系入学。富樫研究室に所属。流体力学的観点からドローンの適用拡大の研究を推進中。主に，ドローンによる CO_2 検知法，飛行しているドローンからの流体音による状態診断の開発に取り組んでいる。
E-mail：s23a362b@kokushikan.ac.jp

富樫　盛典
1995 年 3 月 東京大学大学院工学系研究科機械工学専攻博士課程修了，博士（工学）。1995 年 4 月（株）日立製作所機械研究所に入社。研究室長，主管研究員を歴任。日本機械学会フェロー，日本流体力学会フェロー。2020 年 4 月より国士舘大学理工学部機械工学系の教授として着任。流体力学的観点からドローンの適用拡大の研究を推進中。JUIDA 無人航空機操縦士，一等無人航空機操縦士（国家資格）。
E-mail：togashis@kokushikan.ac.jp

ドローンに対する感性評価のための実機とCGにおける乖離の統計分析

草野　智[*1]，福原　悠介[*2]，佐々木康雄[*3]，満倉　靖恵[*4]，
上出　寛子[*5]，原　進[*3]
名古屋大学大学院工学研究科機械システム工学専攻[*1]
名古屋大学工学部機械航空宇宙工学科[*2]
名古屋大学大学院工学研究科航空宇宙工学専攻[*3]
慶應義塾大学理工学部システムデザイン工学科[*4]
京都大学大学院法学研究科[*5]

UAMを普及させるためには，UAMの飛行が人々の無意識下にある感性に与える影響を正確に評価する必要がある．しかしながら，現実にUAMを飛行させて人々の無意識下の感性を計測するのには高いコストがかかる．そこで，現実にUAMを飛行させる代わりに，UAMが飛行するCGを人々に見せたときの無意識下での感性を計測することが考えられる．ここで問題となるのは，現実とCGでのUAMの飛行によって人々が受ける感性に乖離がある可能性があることである．先行研究ではUAMの代わりに小型のドローンを利用して，感性の乖離の評価を試みた．しかしながら，サンプルサイズが小さいため，統計的な分析をほとんど行うことができなかった．本研究では，先行研究よりも多くの実験参加者を集め，現実とCGのドローンの飛行によって生じる感性を計測した．そして，統計的仮説検定を行うことで，二つの感性指標に対して，感性の乖離があることを示した．また，感性の乖離が示唆されなかったそのほかの感性指標に対しては，乖離が検出されるために必要なサンプルサイズの推定を行った．

Keywords: ディスクレパンシー，脳波計測，統計的仮説検定，社会受容性，UAM

Statistical Analysis of Discrepancies Between Actual and Computer Graphics Drones for Evaluating Sensitivity Toward Drones

Satoshi Kusano[*1], Yusuke Fukuhara[*2], Yasuo Sasaki[*3], Yasue Mitsukura[*4],
Hiroko Kamide[*5], Susumu Hara[*3]
Department of Mechanical Systems Engineering, Nagoya University[*1]
Department of Mechanical and Aerospace Engineering, School of Engineering, Nagoya University[*2]
Department of Aerospace Engineering, Nagoya University[*3]
Department of System Design Engineering, Keio University[*4]
Graduate School of Law, Kyoto University[*5]

To promote UAM adoption in society, it is necessary to accurately assess the impact of UAM flights on people's unconscious sensibilities. However, flying UAMs to measure these unconscious sensibilities incurs high costs. Therefore, instead of flying actual UAMs, it is conceivable to measure the unconscious sensibilities when people view CG of flying UAMs. The issue here is the potential discrepancy in the sensibilities people experience when exposed to real versus CG UAM flights.

Previous studies attempted to evaluate this sensitivity discrepancy by using a small drone instead of UAMs. However, they could perform little statistical analysis due to the small sample size. This study gathered a larger number of participants than previous research and measured the sensitivity responses elicited by the flight of real and CG drones. Statistical hypothesis testing was then performed, and discrepancies were detected in two sensitivity indices. Furthermore, for the other sensitivity indices where no discrepancy was detected, the sample size required to detect a discrepancy was estimated.

Keywords: discrepancy, EEG measurement, statistical hypothesis testing, social acceptance, urban air mobility

1. Introduction

Drones are becoming increasingly prevalent, with industrial drones being utilized in the logistics sector and "urban air mobility (UAM)" expected to be implemented as a next-generation transportation infrastructure. For example, Japan aims to further expand the commercial use of UAM in the late 2020s [1]. Although extensive research and development efforts have been devoted to ensure the safety and performance of these vehicles, relatively little attention has been paid to the issue of social acceptance associated to UAMs. In general, social acceptance is often discussed in terms of technical, institutional, and market-related factors [2]; however, in this study, this term refers specifically to psychological aspects, such as the extent to which citizens can tolerate psychological discomfort due to noise and visual oppression. In the past, insufficient consideration of social acceptance led to public opposition movements following the construction of airports and high-speed rail lines. Therefore, this historical lesson should be carefully considered. To the best of our knowledge, there are no established evaluation criteria for assessing social acceptance. Therefore, facilitating the smooth market introduction of UAM requires establishing an objective evaluation method for social acceptance, defining acceptance criteria and incorporating them into the development process. Hara et al. attempted to objectively evaluate social acceptance by using a simplified EEG-based analyzer, Kansei analyzer, to measure stress levels [3].

A psychosocial survey on noise conducted by Yamauchi et al. indicated that tolerance to stress may vary depending on the purpose of mobility and the stakeholders involved, even if the same type of mobility is considered [4]. In addition, prior studies have attempted to incorporate the subjective stress caused by drone noise into the formulation of operational conditions for drone flights [5]. However, simply setting a uniform noise level and developing technology to meet this threshold does not necessarily improve social acceptance among citizens and users. Therefore, acceptable noise levels for each specific use case and stakeholder group should be explored. To date, such studies have not been sufficiently conducted [6]. To address this gap, Takahara et al. conducted a benefit-effect assessment experiment using scenario-based methods to clarify the acceptable noise levels for each specific use case [7]. The results suggested that in scenarios involving high social significance, such as emergency medical services, the acceptable noise level may be higher than that for more routine uses such as commuting. However, the reliability of the obtained data was insufficient, highlighting the need to improve the experimental environment and investigate the factors contributing to stress. Furthermore, even if the participants can sufficiently imagine the scenarios presented, the discrepancy between the real UAM and computer graphics (CG) used in the experiment cannot be overlooked, making it essential to refine the experimental environment and reduce the discrepancies between real UAM and CG representations.

In this study, conducting experiments using an actual UAM was impractical; therefore, drones were used as substitutes to examine the relevant issues. Specifically, the Kansei analyzer was employed to

evaluate the discrepancy in sensitivity between actual and CG drones. The Kansei analyzer estimates five emotional indices (interest, like, concentration, stress, and calmness) based on characteristic EEG features, which have been empirically associated with physiological and emotional states in previous studies [8, 9, 10]. The advantage of this analyzer over the questionnaire approach is the ability to measure unconscious emotions in real time quantitatively. Quantitative evaluation of the sensitivity discrepancy aids in creating CG that minimizes such discrepancies. Another application of quantified discrepancy is correcting the sensitivity values obtained from CG using the discrepancy values to predict the sensitivity values produced by the actual drone.

Previous studies [11, 12] attempted to statistically evaluate the discrepancy between the sensitivity caused by CG drones and a real drone as in this study. However, since they had a small number of experimental participants (only six), they could not demonstrate that sensitivity discrepancy was significant. In this experiment, by recruiting more participants than the previous studies, we obtained data with a sample size 4.5 times larger than that of the previous studies. Due to this large sample size, significant discrepancies were detected in two sensitivity indices. We consider the causes of the significant differences in the two sensibilities and a method to utilize the obtained discrepancy values.

This paper is organized as follows: Section 2 outlines the Kansei analyzer, which is used for measuring emotion of participants. In Section 3, drones' factors which affect the human sensitivity are explained, and a factor on which we focus is introduced. Section 4 describes the actual drone and CG drones, the experimental protocol, and analysis methods for the experimental data. Section 5 presents the analysis results, Section 6 shows the results of the statistical analysis, and Section 7 discusses these results. Section 8 includes some concluding remarks.

2. Kansei analyzer

The Kansei analyzer used in this study (**Figs.1** and **2**) is a simplified EEG-based analyzer capable of measuring five emotional indices in real-time: interest, like, concentration, stress, and calmness [10]. This real-time capability is particularly useful for performing time-series sensitivity assessments.

The Kansei analyzer estimates the emotional indices from measured EEG signals via relationship equations derived from a long-term accumulated database between EEG signals and the emotional indices. The Kansei analyzer estimates the emotional indices from measured EEG signal. In the estimation process, first, the noises of the EEG signal are removed by using filters such as a Kalman filter. Characteristic features of the EEG signal are then extracted based on Fourier analysis and other methods. The values of the emotional indices are finally computed via equations which express the relationship between the characteristic features and the emotion indices. Here, the relationship between the EEG features and the emotional indices was identified from a database in which pairs of the EEG signals and physiological hormone levels associated with the emotion indices had been collected. See [13] for further details on the estimation process of the Kansei analyzer.

Fig.1 Installation method.

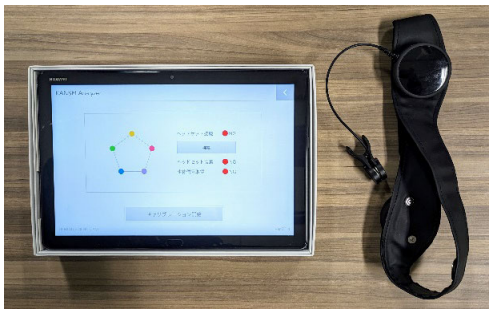

Fig.2 Kansei analyzer.

3. Factors of drones affecting human sensitivity

Evaluating the discrepancies in sensitivity indices (interest, like, concentration, stress, and calmness) between actual and CG drones requires creating a CG representation based on the drones' factors that influence human sensitivity. This section explains the influencing factors based on previous studies.

The first factor is drone noise. Noise is an important contributor to stress caused by drones. Drone noise contains a higher proportion of high-frequency components and pure tones than traffic or aircraft noise in the environment [6]. Thus, drone noise is often perceived as more unpleasant than typical environmental noise. In particular, the rapid modulation of sound caused by the propeller rotation has been reported to intensify this discomfort.

The second factor is drone size. Larger drones are reported to have a stronger visual presence, evoking a greater sense of intimidation and perceived danger [14]. Additionally, larger drones are perceived to be closer in proximity compared to smaller ones, further amplifying psychological stress [15].

The third factor is flight altitude. Drones flying at lower altitudes are associated with increased concerns regarding noise, safety, and invasion of privacy [14].

The final factor is flight speed. Sudden changes in direction and high-speed flights have been identified as stress-inducing factors. Specifically, as flight speed increases, it becomes more difficult for observers to predict the trajectory of the drone, which increases the perceived risk of collision [6].

This study focused on a factor of these: drone noise, which is one of the most frequently reported influential factors affecting human sensitivity. We make three types of CG which simulate flight of an actual drone but have distinct noise levels each other. One type of CG has the same noise level as the flight of the actual drone, and the other two have the smaller and larger noise levels. The sensitivity indices of the participants are measured when the participants watch the flights of the CG and actual drones separately. Then, the discrepancies in the sensitivity indices between the actual and CG drones are analyzed for each noise level of CG.

4. Experimental method and setup

The experiments were conducted with the cooperation of individuals who did not have a deep professional involvement with drones in the context of research or economic activities. Prior to participation, the purpose and procedures of the experiment were thoroughly explained and informed consent was obtained from all participants. This experiment was approved by the Ethics Committee of the Safety and Welfare Committee, Graduate School of Engineering, Nagoya University (Approval Number: 24-18). The participants were recruited through various means, including posting recruitment posters at universities.

4-1 Experimental environment and drone flight path

The actual drone, DJI Mini 4 Pro, used in this experiment and the CG drone are shown in **Figs.4** and **5**, respectively. The experimental environment and flight path are shown in **Figs.6** and **7**, respectively. The DJI Mini 4 Pro [16] is equipped with an omnidirectional vision system and 3D infrared sensing system, enabling detection of obstacles in all directions while hovering or flying outdoors. It is also equipped with an automatic return-to-home (RTH) function. The drone itself is a compact, foldable model, weighing less than 249 g, with dimensions of 148×94×64 mm^3 (length×width×height) when folded (without propellers) and 298×373×101 mm^3 when unfolded (with propellers). The maximum flight time was 34 min using the Intelligent Flight Battery and 45 min using Intelligent Flight Battery Plus. The maximum noise level of the drone at its closest point to the participants (0.8 m in front of them) was 70 dB.

Sensitivity indices were measured over a 20 s period before and after the actual drone started its flight or the CG drone video started playing. The actual drone takes off from the platform at a height of 0.4 m above the ground, ascending to a height of 1.2 m over a period of 5 s. It then approaches the participant over a span of 15 s and stops 0.8 m in front of the participant. During this 20 s period, the participants' EEG data are measured using the Kansei analyzer. After the drone stops, the drone hovers for 2 s at 0.8 m in front of the participant and then flies to the participant's right side until it disappears from view. The CG drone was created based on the specified dimensions, maximum noise level at the closest point (0.8 m in front of the participant), and flight path of the actual drone.

Fig.4 Actual drone.

Fig.5 CG drone.

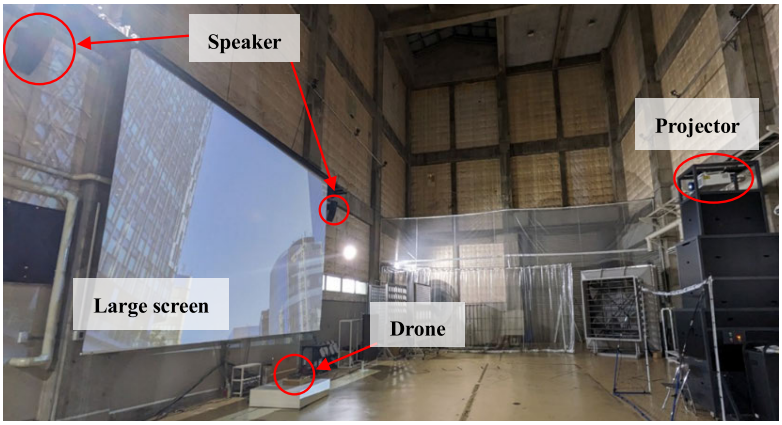

Fig.6 Experimental environment.

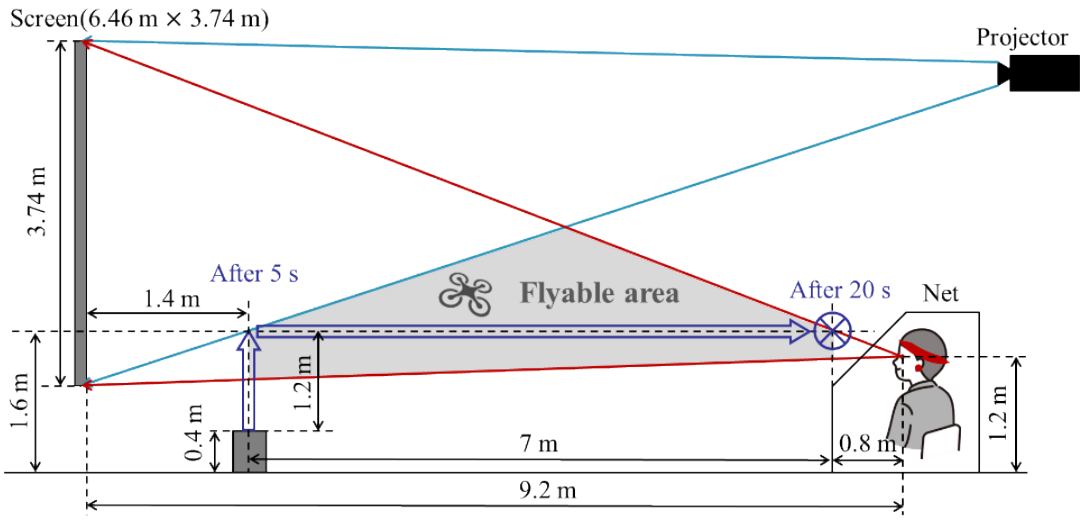

Fig.7 Flight path.

4-2 Experimental protocol

The experimental procedure is illustrated in Fig.8. Each participant was asked to view four types of drones: actual, CG1, CG2, and CG3. To ensure sufficient time for rest and administering the questionnaires, an interval was inserted between each viewing session. The overall questionnaire consisted of (i) a preliminary questionnaire addressing participant attributes (e.g., age, sex, prior experience with drones, and living environment), (ii) an in-situ questionnaire evaluating the stress experienced while viewing each drone (e.g., perceived risk of personal safety, noise, and visual impact), and (iii) a post-experiment questionnaire asking participants to compare the actual drone with the three CG drones, focusing on differences in appearance, noise, and sense of realism. The purpose of these questionnaires was to identify factors other than the drones themselves that might influence the participants' sensitivity and to clarify potential areas for improving the experimental environment. Furthermore, to account for order effects, the presentation order of the four drones was randomized.

The maximum noise levels in the flights of the actual and CG drones are shown in Table 1. The sensitivity indices were measured during each flight of the CG drones with distinct noise levels and the actual drone. Specifically, CG1 was a CG drone with a maximum noise level of 60 dB, which is 10 dB lower than that of the actual drone; CG2 had a maximum noise level of 70 dB, identical to that of the actual drone; and CG3 had a maximum noise level of 80 dB, 10 dB higher than that of the actual drone. The sound for the CG drones was created by recording the flight sound of an actual drone and then processing and editing it. Noise levels were measured according to the A-weighting characteristic [17], which reflects the sensitivity of the human ear to sound, whereby lower sound levels and frequencies are perceived as less intense by human listeners.

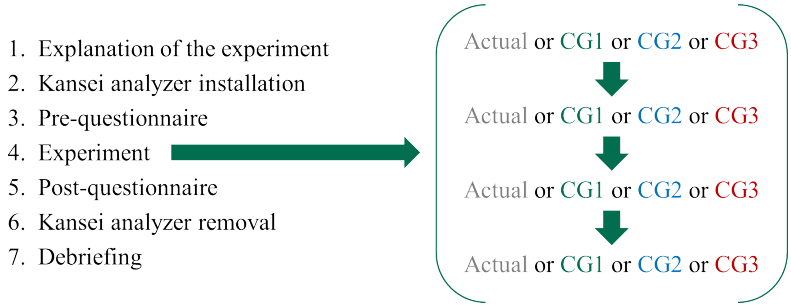

Fig.8 Experimental flow.

Table 1 Experimental group.

Actual drone	CG1 (Small)	CG2 (Medium)	CG3 (Large)
70	60	70	80

5. Classification method for analysis results using statistical hypothesis testing

5-1 Preprocessing and definition

This section explains the analytical method using the sensitivity data measured by the Kansei analyzer. This analysis is intended to evaluate the discrepancy between the actual drone and the CG drones with distinct noise levels. Sensitivity indices measured for 20 s before and during the flights were weighted based on the mean and standard deviation of each sensitivity index. Weighting was applied to account for the varying difficulty of the sensitivity changes depending on the initial value. For example, a change from 50% to 60% is relatively easy to achieve, whereas a change from 90% to 100% is considerably more difficult. This difficulty was reflected in the data through weighting. Let a_t denote the sensitivity value at time t [s], μ the mean value, and σ the standard deviation. The weighting coefficient

w_t was determined according to the following rule:

$$w_t = \begin{cases} 1 & |a_t - \mu| < \sigma \\ 1.5 & \sigma \le |a_t - \mu| < 2\sigma \\ 2 & 2\sigma \le |a_t - \mu| < 3\sigma \\ 2.5 & 3\sigma \le |a_t - \mu| \end{cases}. \tag{1}$$

These weighting coefficients were determined empirically based on previous studies and experience. The sensitivity measurements obtained from the Kansei analyzer are shown in **Fig.9**. The weighted averages of the sensitivity values for the *i*-th participant during the 20 s before and after flight start (or CG playback start) are expressed by

$$\bar{a}_{i,1} = \frac{\sum_{t=t_s-20}^{t_s} w_t a_t}{\sum_{t=t_s-20}^{t_s} w_t}, \tag{2}$$

$$\bar{a}_{i,2} = \frac{\sum_{t=t_s}^{t_s+20} w_t a_t}{\sum_{t=t_s}^{t_s+20} w_t}, \tag{3}$$

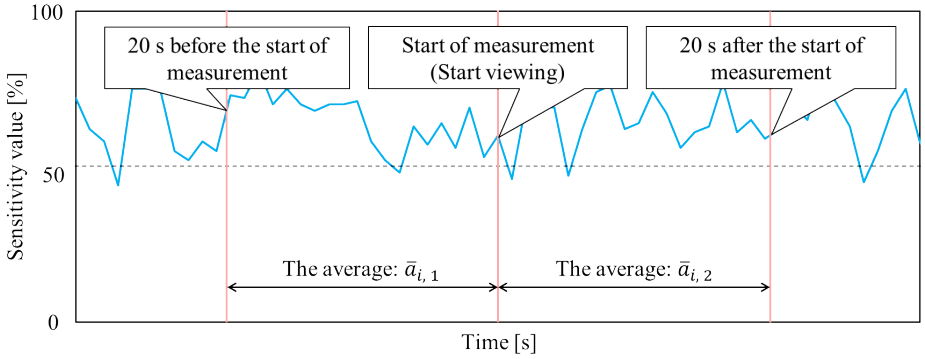

Fig.9 Sensitivity measurement using the Kansei analyzer.

respectively. Here, t_s [s] denotes the time at which drone flight (or CG playback) begins. Using Eqs. (2) and (3), the sensitivity variation for the *i*-th participant when observing drone type *j* is expressed as follows:

$$x_i^j = \bar{a}_{i,2} - \bar{a}_{i,1} \quad (j = 0, 1, 2, 3), \tag{4}$$

where *j*=0, 1, 2, 3 represent actual, CG1, CG2, and CG3 drones, respectively. Using Eq. (4), the sensitivity discrepancy between the actual and each CG drone *j* for the *i*-th participant can be expressed as

$$D_i^j = x_i^j - x_i^0 \quad (j = 1, 2, 3). \tag{5}$$

This equation enables us to evaluate the discrepancies in sensitivity indices of each participant regarding actual and CG drones. Using Eq. (5), the average sensitivity discrepancy between the actual and each CG drone over participants was defined as

$$D_{\mathrm{Ave}}^j = \frac{1}{N}\sum_{i=1}^{N} D_i^j \quad (j = 1, 2, 3). \tag{6}$$

In Eq. (6), if average sensitivity discrepancy D^j_{Ave} is close to zero, the CG type j is interpreted as having a smaller discrepancy from the actual drone. Furthermore, by refining the CG drone so that the value of Eq. (6) approaches zero, a simulator capable of appropriately assessing the sensitivity values can be developed.

5-2 Statistical hypothesis testing

We first explain basics of statistical hypothesis testing. In the statistical hypothesis testing, for example, when an analyzer believes that a difference exists between the means of two populations, the analyzer determines truth or falsehood from the samples from the two populations. In this process, the analyzer first formulates a hypothesis stating the opposite of what to assert—namely, that "there is no difference in the means." If the probability of "no difference in the means" is low, the analyzer concludes that "there is a difference in the means." This probability is called the p-value. The threshold of the probability is called the significance level and denoted by α. If the condition $p \leq \alpha$ holds, the analyzer concludes that there is a significant difference between the means of the two populations. In this study, a popular setting of the significance level, α=0.05, was adopted.

To examine the differences in the mean sensitivity variation values across different drone types, analysis of variance (ANOVA) and multiple comparison tests were conducted. When a significant difference is detected in ANOVA, Tukey's honest significant difference (HSD) test is subsequently performed as a multiple comparison test to identify the pairs of conditions that exhibit significant differences. The following subsections outline the ANOVA and the Tukey's HSD test.

For the analysis, we assume the following model:

$$x_i^j = \mu + \mu_i + \mu^j + \epsilon_i^j, \tag{7}$$

where μ is the population mean, $\mu+\mu_i$ is the population mean for group i, $\mu+\mu^j$ is the group mean with respect to individual j, and ϵ_i^j is the observation noise which is the i.i.d. Gaussian random variable with zero mean and some variance. In model (7), the two factors of the groups (CG1, CG2, CG3, and actual drones) and the individuals are considered. Since sensibilities differ from person to person, it is natural to assume the model incorporating the individual factor.

5-2-1 ANOVA

Although t-tests are commonly used to test the differences between the means of the two groups, applying pairwise tests to more than two groups increases the overall significance level and leads to the problem of multiplicity [18]. ANOVA is a statistical method used to analyze data in which the sample is obtained under three or more conditions [19]. This method evaluates whether there are statistically significant differences in mean values across all conditions.

This study employs ANOVA under model (7) to compare the means of the changes in sensitivity indices elicited by the flights of four types of drones. In the ANOVA, the null hypothesis and the alternative hypothesis are the followings:

- H_0: There are no statistically significant differences between all pairs of the mean sensitivity variations for four drone types.
- H_1: There is at least one pair of the mean sensitivity variations for four drone types that shows a statistically significant difference.

Rejecting the null hypothesis supports the alternative hypothesis.

The procedure for the ANOVA is explained below. ANOVA under model (7) is based on the two-way layout design in which factors are the groups and individuals with one measurement per condition. Table 2 shows the definitions of the symbols which are used for explanation of the ANOVA. Here, $\bar{x}_i$ denotes the sample mean for group i, $\bar{x}^j$ denotes the sample mean for individual j, $\bar{x}$ denotes the overall

mean value, n denotes the sample size for any group, N denotes the total sample size for all data, and k denotes the number of levels (number of groups). First, to perform the ANOVA, compute the sum of squares, SS, degrees of freedom, df, and mean square MS for the group factor, individual factor, error, and total. Then, F value with respect to the groups is computed as follows:

$$f = \frac{MS_{\mathrm{G}}}{MS_{\mathrm{E}}}. \tag{8}$$

Next, based on the group-factor degrees of freedom, df_{G}, and the error degrees of freedom, df_{E}, the critical value $F(df_{\mathrm{G}}, df_{\mathrm{E}}; \alpha)$ is computed from the F distribution table. When the condition $f > F(df_{\mathrm{G}}, df_{\mathrm{E}}; \alpha)$ holds, the probability of the sample occurring under the null hypothesis is less than α. In this case, the null hypothesis is rejected, and it is concluded that there is significant difference between at least one of all pairs. However, ANOVA cannot determine which specific groups differ significantly from one another.

Table 2 Elements required for two-way ANOVA computation.

Source	SS	df	MS
Group	$\sum_{i=0}^{k-1} n(\bar{x}_i - \bar{x})^2$	$k-1$	$\frac{SS_{\mathrm{G}}}{df_{\mathrm{G}}}$
Individual	$\sum_{j=1}^{n} k(\bar{x}^j - \bar{x})^2$	$n-1$	$\frac{SS_{\mathrm{I}}}{df_{\mathrm{I}}}$
Error	$\sum_{i=0}^{k-1}\sum_{j=1}^{n}\left(x_i^j - \bar{x}_i - \bar{x}^j + \bar{x}\right)^2$	$N-k-n+1$	$\frac{SS_{\mathrm{E}}}{df_{\mathrm{E}}}$
Total	$SS_{\mathrm{G}}+SS_{\mathrm{I}}+SS_{\mathrm{E}}$	$N-1$	-

5-2-2 Tukey's HSD test

Tukey's HSD is a multiple comparison test applied after ANOVA detects significant differences between any pair of the groups [18]. This method was used to compare the mean values between each pair of groups (the actual drone, CG1, CG2, and CG3) to determine whether the differences between the pairs are statistically significant. Specifically, the test evaluates ${}_kC_2$ pairs with respect to the null hypothesis H_0 and alternative hypothesis H_1:

- H_0: There is no statistically significant difference in the mean sensitivity variation between the selected pairs of groups.
- H_1: There is a statistically significant difference in the mean sensitivity variation between the selected pairs of groups.

If the t-tests are performed repeatedly for all possible pairs, the multiplicity problem can arise, increasing the risk of Type I errors (false positives). A key feature of Tukey's HSD test is that it strictly controls the significance level for each pairwise comparison, thereby reducing the risk of Type I error caused by multiple comparisons.

The general procedure for Tukey's HSD test is explained below. First, the standard error of the mean differences between groups is computed as follows:

$$SE = \sqrt{\frac{2MS_{\mathrm{E}}}{n}}. \tag{9}$$

Subsequently, based on the number of levels k, error degrees of freedom df_E, and significance level α, the critical value $Q(k, df_E; \alpha)$ is obtained from the q-distribution table. This critical value is then used to determine whether a significant difference exists between the selected pairs of groups. Specifically, the test statistic $t_{ii'}$ for groups i and i' is computed as follows:

$$t_{i\,i'} = \frac{|\bar{x}_i - \bar{x}_{i'}|}{SE} \tag{10}$$

The computed $t_{ii'}$ is then compared with the critical value $Q(k, df_E; \alpha)$. If the condition $\sqrt{2}t_{ii'} > Q(k, df_E; \alpha)$ is satisfied, the null hypothesis is rejected, indicating a statistically significant difference between the two groups.

In the right-hand side of Eq. (10), the only variables with respect to groups i and i' are the sample means $\bar{x}_i$ and $\bar{x}_{i'}$. Hence, equation (10) is rearranged to define the HSD value as

$$\left|\bar{x}_i - \bar{x}_{i'}\right| > Q\left(k, df_E; \alpha\right)\frac{SE}{\sqrt{2}} = HSD. \tag{11}$$

The HSD value serves as the critical value for determining the presence or absence of a significant difference based on the difference between the mean values of the selected pair of groups. In comparing the difference between the means of the two groups with the HSD value, if the condition in Eq. (11) is satisfied, the null hypothesis is rejected, indicating that a statistically significant difference exists between the selected pairs of groups. Once the HSD value is computed, determining significance requires only a comparison of the group mean differences. Thus, Eq. (11) is more convenient than Eq. (10).

The mean difference between groups i and i', $\mu_i - \mu_{i'}$, is estimated by the sample mean difference $\bar{x}_i - \bar{x}_{i'}$. The confidence interval with the confidence level $1-\alpha$ is given by

$$\bar{x}_i - \bar{x}_{i'} - HSD < \mu_i - \mu_{i'} < \bar{x}_i - \bar{x}_{i'} + HSD. \tag{12}$$

From Eq. (12), we can observe that HSD represents the half width of the confidence interval.

6. Analysis results obtained from the Kansei analyzer

Appropriate evaluation of the effects of drones on sensitivity using the Kansei analyzer requires that the influence of factors unrelated to drones be eliminated. As described in Section 3-2, the purpose of the questionnaire was to identify non-drone factors affecting sensitivity and identify potential improvements to the experimental environment. Therefore, the following discussion focuses on the results obtained using the Kansei analyzer.

The experiment participants consisted of 28 individuals aged 19 to 29, including 20 males and 8 females. All participants were university or graduate students. Among the 28 participants, one was involved with drones through research or economic activities. Since this experiment targeted individuals with no prior involvement with drones, the data of the participant was excluded from data for the statistical analysis. Consequently, we used data of the 27 participants.

The results of the ANOVA and Tukey's HSD test for the average sensitivity variation values are shown in **Tables 3–9**. Note that the results of Tukey's HSD test are only provided for sensitivity indices for which the two-way ANOVA detects the significant differences. The average discrepancy values in interest, like, concentration, stress, and calmness indices for different noise levels are shown in **Figs.11** (a)–(e).

Table 3 Results of ANOVA for interest.

Factor	SS_G	MS_G	df_G	df_I	f	p value	Effect size	Power
Drone type	602.550	200.850	3	78	3.368	0.023	0.360	0.766

Table 4 Results of Tukey's HSD test for interest.

Contrast	$\bar{x}_i - \bar{x}_{i'}$	SE	HSD	$t_{ii'}$	p value
CG1 (S) – Actual drone	-6.488	2.1	5.5	3.087	0.015
CG2 (M) – Actual drone	-4.329	2.1	5.5	2.060	0.176
CG3 (L) – Actual drone	-4.409	2.1	5.5	2.098	0.163
CG1 (S) – CG2 (M)	-2.160	2.1	5.5	-1.028	0.734
CG1 (S) – CG3 (L)	-2.079	2.1	5.5	-0.989	0.756
CG2 (M) – CG3 (L)	0.081	2.1	5.5	0.0380	1.000

Table 5 Results of ANOVA for like.

Factor	SS_G	MS_G	df_G	df_I	f	p value	Effect size	Power
Drone type	244.070	81.358	3	78	1.218	0.309	0.216	0.330

Table 6 Results of ANOVA for concentration.

Factor	SS_G	MS_G	df_G	df_I	f	p value	Effect size	Power
Drone type	690.380	230.130	3	78	1.614	0.193	0.249	0.428

Table 7 Results of ANOVA for stress.

Factor	SS_G	MS_G	df_G	df_I	f	p value	Effect size	Power
Drone type	149.470	49.822	3	78	0.677	0.569	0.161	0.195

Table 8 Results of ANOVA for calmness.

Factor	SS_G	MS_G	df_G	df_I	f	p value	Effect size	Power
Drone type	112.810	37.602	3	78	5.104	0.003	0.443	0.923

Table 9 Results of Tukey's HSD test for calmness.

Contrast	$\bar{x}_i - \bar{x}_{i'}$	SE	HSD	$t_{ii'}$	p value
CG1 (S) – Actual drone	2.615	0.739	1.9	-3.539	0.004
CG2 (M) – Actual drone	2.295	0.739	1.9	-3.107	0.014
CG3 (L) – Actual drone	1.255	0.739	1.9	-1.698	0.331
CG1 (S) – CG2 (M)	0.319	0.739	1.9	0.432	0.973
CG1 (S) – CG3 (L)	1.360	0.739	1.9	1.841	0.262
CG2 (M) – CG3 (L)	1.040	0.739	1.9	1.408	0.498

7. Discussion on analysis results obtained from the Kansei analyzer

7-1 Discussion on like, concentration, and stress

No significant difference between any pair of the actual and CG drones was detected in the like,

concentration, and stress indices. In other words, in these indices, there is no significant discrepancy between the actual drone and each CG drone, and there is no significant difference between the CG drones with distinct signal levels. At first glance from **Figs.11** (b)–(d), there seem to be discrepancies in the like, concentration, and stress indices between CG drones and real drones, and there seems to be tendencies for changes in these sensitivities regarding noise levels. For example, stress seems to increase as noise levels rise. However, the ANOVA results indicate that such apparent discrepancies or tendencies might be due to chance.

We cannot conclude that there is no difference in the like, concentration, and stress indices between the actual and CG drones from the ANOVA results. Rather, since all the actual and CG drones are fundamentally different from each other, it is more natural to assume that sensitivity affected by each drone differs. The lack of significant differences detected by ANOVA is likely due to insufficient sample size. Increasing the sample size reduces the uncertainty of the mean and makes it easier to detect a significant difference, in general.

We computed the sample sizes required for ANOVA to detect significant differences in like, concentration, and stress indices. To this end, we used a software, G*Power of version 3.1 [20]. G*Power

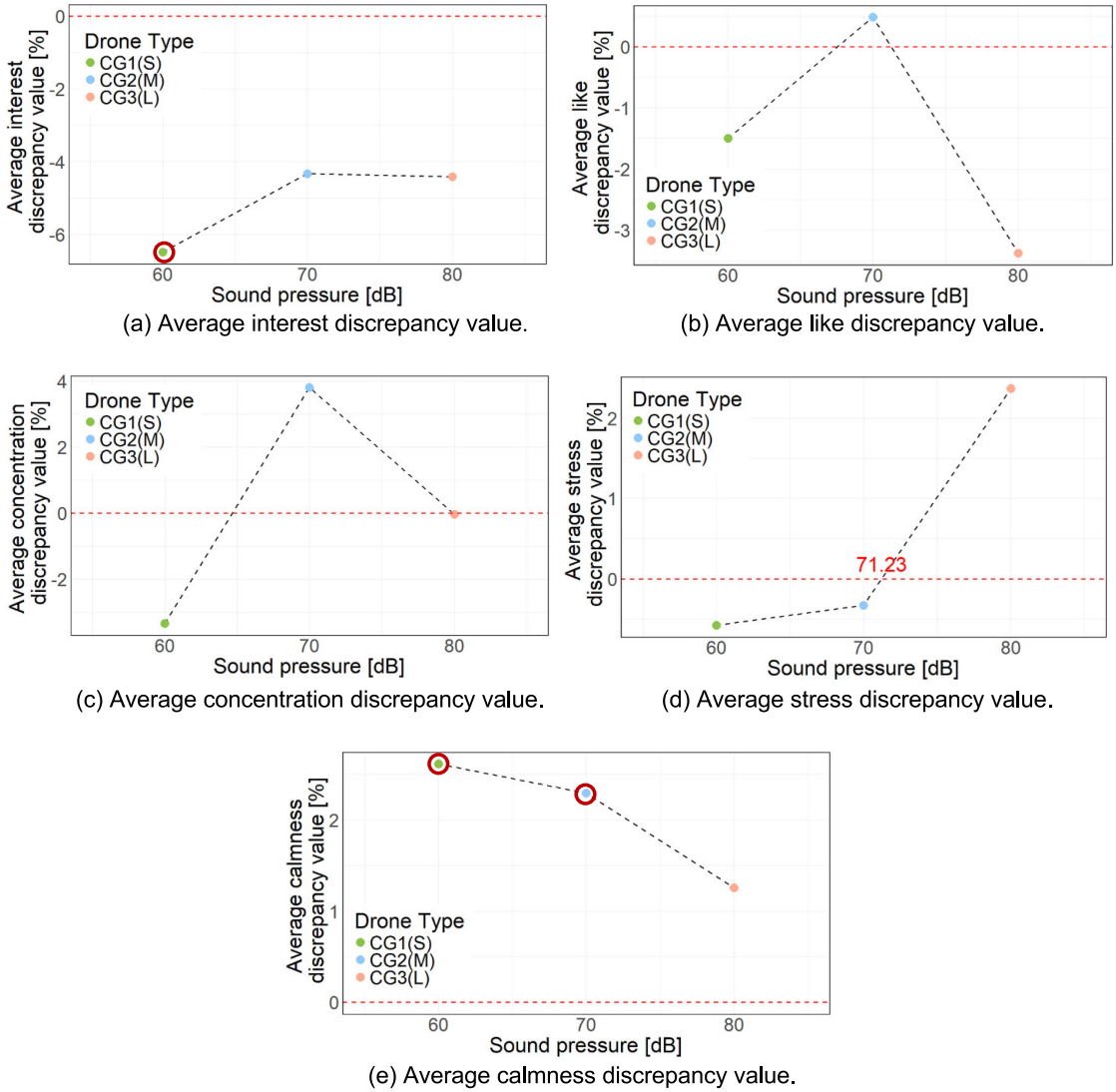

Fig.11 Results of average sensitivity discrepancy values for different noise levels. Red circles indicate conditions showing statistically significant differences from the actual drone according to Tukey's HSD test ($p < 0.05$).

can compute the minimum sample size required to detect a statistically significant result while meeting specified power and significance level in specified statistical analysis [21, 22]. The significance level, power, and effect size must be specified to compute the minimum sample size. The significance level and the effect size were set at the values obtained by the ANOVA for each sensitivity index. We set the power at 0.8.

Table 10 shows the minimized sample sizes for like, concentration, and stress indices. It is evident that detecting significant differences in the three indices would require participants considerably larger than the 27 participants in the experiment of this study. Note that the numbers shown in Table 10 represent the sample size required to detect a significant difference for any pair of the drones. A larger sample size is necessary to detect a significant difference for a specific pair of drones.

Table 10 Sample sizes required for ANOVA to detect significant differences in like, concentration, and stress indices.

Like	Concentration	Stress
65	50	110

7-2 Discussion on interest and calmness

Significant differences in interest and calmness were detected in the ANOVA, and the Tukey's method was used for the two indices. The Tukey's test detected a significant difference in interest between the CG1 and actual drones and significant differences in calmness between the CG1 and actual drones and between the CG2 and actual drones. On the other hand, the Tukey's test did not detect any significant difference in interest and calmness indices between any pair of the CG drones. Therefore, no significant changes in sensitivity attributable solely to noise level were observed for all indices examined in this study.

The mean difference in interest between the actual and CG1 drones is −6.5. The mean differences in calmness between the actual and CG1 drones and between the actual and CG2 drones are 2.6 and 2.3, respectively. Since these differences are significant, it is strongly recommended to correct changes in the sensitivity values due to the CG drone when changes in the sensitivity values are predicted from the changes due to the CG drone. For example, let us consider a scenario where an experiment was conducted showing only the CG2 drone to a student different from the participants in this experiment. We know there is a discrepancy in interest between the actual and CG2 drones, and we can correct the measured change in interest by 2.3 for predicting the change in interest due to the actual drone. Flying a drone requires large open spaces and safety equipment, which adds to the burden of conducting experiments. Being able to predict changes in sensitivity due to actual drone flight by using CG can help reduce this experimental burden.

The Tukey test results show that the actual drone attracts participants' interest and causes them to lose participants' calmness more than CG1. It also shows that the actual drone causes participants to lose calmness more than CG2. It is natural for participants who usually see drones to be interested in the drones, and to lose calmness when the drone approaches with loud noises. The Tukey test results suggest that the magnitude of these changes in interest and calmness differs between the two CG drones and the actual drone.

It is not unreasonable to assume that as interest of the participants increases, their attention and arousal levels also rise, and their calmness decreases. The discrepancy between interest and calmness observed in CG1 might be related to this connection between interest and calmness.

The significant difference in sensitivity between the CG and actual drones is presumed to arise from differences in auditory and visual stimuli. Regarding visual perception, humans can perceive objects in

three dimensions using their eyes. The CGs projected on the screen reproduced the actual drone's size and shape in two dimensions. They did not, however, reproduce the drone's three-dimensionality. Regarding auditory perception, humans can locate sound sources in three-dimensional space using their ears. The sound of the drone reproduced in the CGs was set to increase in volume as it approaches. However, the CGs did not accurately reproduce the sound of the drone to the extent that its position can be discerned. This incompleteness in CG reproduction might have dulled changes in interest and calmness.

8. Conclusion

8-1 Summary

In this study, we conducted an experiment to evaluate the sensitivity discrepancies between actual and CG drones with varying noise levels. Three CG types were used: CG1 with low noise level, CG2 with medium noise level, and CG3 with high noise level. Here, CG2's noise level was equivalent to that of the actual drone. 27 participants observed flights of the actual drone and the three CG types, and changes in their sensitivity during each flight were measured by the Kansei analyzer. After processing the measured sensitivities, Tukey's test was used to examine the discrepancies in the sensitivities under the significant level α=0.05. The results showed there was a discrepancy in calmness between the CG1 and actual drones, and between the CG2 and actual drones. Additionally, there was a discrepancy in interest between the CG1 and actual drones. These results suggest that improving the CG and experimental environment is necessary to replace the actual drone with CG drones.

8-2 Future perspectives

The discrepancy between real and CG drones is thought to arise because they provide different stimuli to participants. Many elements cannot be adequately reproduced in the current experimental environment, such as the wind generated by the drone, vibration of the drone during approach, and overall sense of presence. These issues represent important challenges for future research. Although the audio source used for the CG drones was recorded from the actual sound of the approaching drone, differences between the actual and CG drones can still be perceived based on static noise from the speakers and sound reflections in the experimental space. To address this issue, further improvements in sound quality, such as introducing spatial audio technology, are necessary to make the CG drone sound more closely resemble the actual sound of the drone. With regard to the CG animation, its quality must also be improved to better replicate the inherent vibration and dynamic motion unique to actual drones. In addition, the use of two-dimensional CG animations may have fundamental limitations in enhancing the sense of presence in experimental environments. Introducing vertical reality (VR) goggles can significantly enhance the sense of presence and improve the representation of visual factors, such as perceived danger and immersion, when the drone approaches. This would allow the development of a simulator that more closely replicates the experience of observing an actual drone. However, the introduction of VR goggles presents new challenges, including potential interference with the Kansei analyzer, discomfort caused by wearing the goggles, and changes in the questionnaire response process. These factors require a comprehensive revision of the experimental protocol.

This study addressed sensitivity caused by flight of the small drone. Significant discrepancies are likely to occur unless the simulator quality is high in UAMs as well as the small drone. Resolving the above issues and constructing a simulator for UAMs with significantly small discrepancies is a future challenge. Utilizing such a simulator will enable accurate estimation of unconscious changes in sensitivity during UAM flight. This will be useful when evaluating social acceptability of UAMs.

Acknowledgement

The authors would like to thank Kengo Tatsuta for technical assistance regarding G*Power.

Received：January 6, 2026
Accepted：February 6, 2026

References

[1] Ministry of Economy, Trade and Industry : “Advanced Air Mobility Roadmap (in Japanese)”, Public-Private Committee for Advanced Air Mobility, 2022.
[2] Matsuoka, S.: “Social Innovation and Regional Sustainability–Fostering Placemaking and Social Acceptance (in Japanese)”, Yuhikaku, 2018.
[3] Hara, S., Mitsukura, Y., and Kamide, H.: “Noise-Induced Stress Assessment —On the Difference Between Questionnaire-Based and EEG Measurement-Based Evaluations—”, *Technical Journal of Advanced Mobility*, Vol. 3-6, pp. 81–90, 2022.
[4] Yamanouchi, K., Hisata, M., and Yamamoto, K.: “A study of psychosocial factors affecting community noise annoyance (in Japanese)”, *Comprehensive Urban Studies*, Vol. 18, pp. 65–87, 1983.
[5] Torija, A. J. and Nicholls, R. K.: “Investigation of Metrics for Assessing Human Response to Drone Noise”, *International Journal of Environmental Research and Public Health*, Vol. 19–6, 3152, 2022.
[6] Shaffer, B., Pieren, R., Heutschi, K., Wunderli, J., and Becker, S.: “Drone Noise Emission Characteristics and Noise Effects on Humans—A Systematic Review”, *International Journal of Environmental Research and Public Health*, Vol. 18-11, 5940, 2021.
[7] Hara, S., Kusano, S., Mitsukura, Y., Kamide, H., and Sasaki, Y.: “Development of Benefit-Effect Assessment Method for Improving Social Acceptance of Urban Air Mobility”, *Journal of Air Transportation*, pp. 1–11, 2025.
[8] Sato, T., Mitsukura, Y., and Toma, T., “Real-time Kansei analysis during communication using a simplified EEG,” *Emotional Engineering: Understanding Motivation*, Springer, Vol. 6, pp. 63–73, 2017.
[9] Zhou, Z., Cheng, J., Wei, W., and Lee, L., “Validation of evaluation model and evaluation indicators comprised Kansei engineering and eye movement with EEG: an example of medical nursing bed,” *Microsystem Technologies*, Vol. 27, pp. 1317–1333, 2021.
[10] Mitsukura, Y.: “How Brain Waves Hint at Early Signs of Dementia”, *Nature Portfolio*, 2024.
[11] Fukuhara, Y., Kusano, S., Hara, S., Mitsukura, Y., and Kamide, H.: “Evaluation of Discrepancy Between Real Flight and CG for Stress Analysis Using EEG Measurement in Drone Flying Environment (in Japanese)”, *Proceedings of the 61st JSASS Autumn Joint Conference of Chubu and Kansai Branches*, C2, 2024.
[12] Kusano, S., Fukuhara, Y., Hara, S., Mitsukura, Y., and Kamide, H.: “Discrepancy Evaluation Between Actual and Computer Graphics Drones for Stress Analysis by EEG Measurement”, *Technical Journal of Advanced Mobility*, Vol. 6-2, pp. 2–11, 2025.
[13] Mitsukura, Y.: “KANSEI Analyzing by EEG”, *The journal of the Institute of Electrical Engineers of Japan*, Vol. 136, No. 10, pp. 687–690, 2016.
[14] Bretin, R., Khamis, M., and Cross, E.: ““Do I Run Away?”: Proximity, Stress and Discomfort in Human-Drone Interaction in Real and Virtual Environments”, *Human-Computer Interaction – INTERACT 2023*, Springer, pp. 525–551, 2023.
[15] Ramos-Romero, C., Green, N., Roberts, S., Clark, C., and Torija, A. J.: “Requirements for Drone Operations to Minimise Community Noise Impact”, *International Journal of Environmental Research and Public Health*, Vol. 19-15, 2022.
[16] DJI: “DJI Mini 4 Pro”, https://www.dji.com/jp/mini-4-pro, (Accessed: Sep. 26, 2024).
[17] NTi Audio: “Frequency Weightings for Sound Level Measurements”, https://www.ntiaudio.com/en/support/knowhow/frequency-weightings-for-sound-level-measurements, (Accessed: Jul. 9, 2024).
[18] Ogata, H.: “Statistical multiplicity problems and methods for multiple comparisons (in Japanese)”, *Japanese Journal of Health Education*, Vol. 31-3, pp. 173–179, 2023.
[19] Kyushu University Library: “Learning statistics through manual calculation and R: One-way repeated measures ANOVA”, https://guides.lib.kyushu-u.ac.jp/statistics/within_ANOVA, (Accessed: Jan. 17, 2025).
[20] Heinrich-Heine-Universität Düsseldorf: “G*Power”, https://www.psychologie.hhu.de/arbeitsgruppen/allgemeine-psychologie-und-arbeitspsychologie/gpower, (Accessed: Dec. 24, 2025).

[21] Faul, F., Erdfelder, E., Lang, A.-G., and Buchner, A., "G*Power 3: A flexible statistical power analysis program for the social, behavioral, and biomedical sciences" *Behavior Research Methods*, Vol. 39, pp. 175–191, 2007.
[22] Faul, F., Erdfelder, E., Buchner, A., and, Lang, A.-G., "Statistical power analyses using G*Power 3.1: Tests for correlation and regression analyses" *Behavior Research Methods*, Vol. 41, pp. 1149–1160, 2009.

Satoshi KUSANO

He received the B.E. degree from the Department of Fundamental Engineering, Faculty of Engineering, Utsunomiya University in 2023. In the same year, he entered the Master's Program in Mechanical Systems Engineering at the Graduate School of Engineering, Nagoya University. His research interests include social acceptance of UAM.

Yasuo SASAKI

He received the Ph.D. degree from Nagoya University, Japan, in 2022. After serving as a JSPS Research Fellow, a Project Assistant Professor at the Graduate School of Engineering, Tohoku University, and a Project Assistant Professor at the Graduate School of Engineering, Nagoya University, he became an Assistant Professor in the Department of Aerospace Engineering at the Graduate School of Engineering, Nagoya University in 2024.
E-mail: sasaki.yasuo.g8@f.mail.nagoya-u.ac.jp

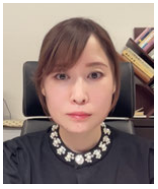

Hiroko KAMIDE

She completed a Ph.D. in Human Sciences at Osaka University in 2008. From 2009 to 2015, she served as a Specially Appointed Assistant Professor at the Graduate School of Engineering Science, Osaka University. From 2015 to 2016, she held the position of Assistant Professor at the Research Institute of Electrical Communication, Tohoku University. From 2016 to 2024, she served as a Designated Associate Professor at the Institute of Innovation for Future Society, Nagoya University. Since 2024, she has been a Program-Specific Associate Professor at the Graduate School of Law, Kyoto University. Research focuses include Human-Robot Interaction (HRI), Buddhist philosophy, and interaction with objects.

Yusuke FUKUHARA

He entered the Department of Mechanical and Aerospace Engineering, School of Engineering, Nagoya University in 2020. His research interests include social acceptance of UAM.

Yasue MITSUKURA

She received the Dr.Eng. degree from the University of Tokushima and the Dr.Med. degree from Keio University, Japan. Since 2011, she has been a Professor with Keio University. Her research interests include bio-signal analysis (EEG, EMG, EOG, ECG, GSR, and body temperature, breath, salivary amylase, NIRS, and fMRI), brain–computer interfaces, Depression, Dementia, and Medical bio-marker. She is a member of SfN, IEE, ARVO.

Susumu HARA

He received the B.S., M.S., and Ph.D. degrees from Keio University, Tokyo, Japan, in 1992, 1994, and 1996, respectively, all in engineering. From 1995 to 2000, he was a Research Fellow with the Japan Society for the Promotion of Science. From 1996 to 2000, he was a Visiting Researcher with the Faculty of Science and Technology, Keio University. From 1998 to 1999, he was a Visiting Scholar with the Department of Mechanical Engineering, University of California, Berkeley. In 2000, he joined the faculty of Toyota Technological Institute, Nagoya, Japan. In 2008, he joined the faculty of Nagoya University, Nagoya, Japan where he is currently a Professor with the Department of Aerospace Engineering, Graduate School of Engineering. His current research interests include motion and vibration control of mechanical structures, nonstationary control methods, control problems of man-machine systems and aerospace equipment.

無人航空機運用における運航リスクおよび労働安全リスクを対象としたリスクアセスメント手法の比較と統合的フレームワークの提案

蓮實　雄大[*1]，中村　瑞穂[*1]，北條理恵子[*2]
是村　由佳[*3]，清水　尚憲[*4]，木村　哲也[*2]
職業能力開発総合大学校[*1]
長岡技術科学大学[*2]
株式会社コレムラ技研[*3]
ジー・オー・ピー株式会社[*4]

無人航空機は新たな技術として社会実装が進む一方，飛行中の運航リスクと，現場における労働安全リスクを統合的に評価する手法が十分に整理されていない。本研究では，飛行許可申請に用いられる運航リスク評価手法（SORA ガイドライン）と，労働安全分野で活用されてきたリスクアセスメント手法（機械包括安全指針）を比較し，適用範囲および実施項目の差異を明らかにする。その結果，両手法は対象とするリスク領域が異なり，一方のみではリスクの見落としが生じる可能性があることを示した。これを踏まえ，SORA ガイドラインを先行実施し，その結果を機械包括安全指針に段階的に反映する統合的リスクアセスメントフレームワークを提案する。本フレームワークを用いることで，無人航空機運用における安全管理実務の効率化が期待される。

Keywords: リスクアセスメント，無人航空機，SORA，労働安全

Comparison of Risk Assessment Methods for Unmanned Aircraft Operations with Operational and Occupational Safety Risks

Yudai Hasumi[*1]，Mizuho Nakamura[*1]，Rieko Hojo[*2]
Yuka Koremura[*3]，Shoken Shimizu[*4]，Tetsuya Kimura[*2]
The Polytechnic University of JAPAN[*1]
Nagaoka University of Technology[*2]
Ballast Division, Koremura Giken Co., Ltd.[*3]
GOP CO., LTD.[*4]

Unmanned aircraft are increasingly deployed as next-generation mobility systems; however, integrated risk assessment methods addressing both flight operations and occupational safety, especially in operational contexts, remain insufficient. This study compares the operational risk assessment method used for regulatory approval（SORA）with a safety risk assessment method used in occupational safety. The comparison clarifies differences in scope and assessment items, indicating that reliance on either method alone may overlook certain risks. Based on these findings, an integrated risk assessment framework is proposed, in which SORA is applied first and its results

are reflected in the occupational safety assessment in stages. This framework will improve the efficiency of safety management of the operations.

Keywords: Risk assessment, UAV, SORA, Occupational Safety

1. は じ め に

1-1 背景と目的

無人航空機は，近年の制御技術の高度化と低コスト化により，研究開発と産業利用が加速し［1, 2］，現在ではインフラ点検，空撮，測量などさまざまな分野で活用が広がり，関連制度の整備が進められている［3, 4］。一方で，無人航空機の普及に伴い，国内外で墜落や人との接触事故が多数報告されており［5–8］，日本でも 2015 年以降無人航空機による事故・インシデントの報告制度が整備され実態把握に取り組んでいる［9］。

日本の現在の航空法では，無人航空機の飛行リスクに応じて飛行カテゴリーが区分されており，特に高リスクな飛行においては飛行申請と許可取得（飛行許可申請）にリスクアセスメントの実施が求められる［10, 11］。リスクアセスメントは，リスクを特定・評価する手法であり，飛行許可申請では SORA（Specific Operation Risk Assessment）を参照して福島ロボットテストフィールドより発行された「安全確保措置検討のための無人航空機の運航リスク評価ガイドライン」に従ってリスクアセスメントを実施し，その結果を反映することが推奨されている［12］。本論文では便宜上，当該ガイドラインを「SORA ガイドライン」と呼ぶ。SORA ガイドラインは，無人航空機操縦者技能証明制度において，一等操縦者技能証明に求められる知識要件を示した教則でも活用が推奨されている［13］。

SORA は各国の航空局が参加する JARUS（Joint Authorities for Rulemaking of Unmanned Systems）が作成したリスクアセスメント手法であり，飛行許可申請のためのツールとして国際的に利用されている［14］。同手法は飛行許可申請のための枠組みとして，第三者に対する地上リスクおよび空中リスクに焦点を当てており，運用者や作業者に関わる労働安全リスクは直接の評価対象外とされている。

しかし，無人航空機の運用は飛行中の運航に限らず，準備，設置，保守，撤去といった作業を含むことから，労働安全の観点からのリスクアセスメントも重要である。空機全般の安全の国際的基盤となる ICAO Safety Management Manual（SMS）では，労働安全は各国の制度に基づき検討する事を求めている［15］。

日本の労働安全分野では，労働安全衛生法によりリスクアセスメントの実施が求められており，機械を使用する作業については，「機械の包括的な安全基準に関する指針」［16］（以下，機械包括安全指針）により，リスクアセスメントを実施することが示されている。無人航空機は機械の定義に該当することから，その運用は同指針の適用範囲に含まれると考えられる。機械包括安全指針は，JIS B 9700（機械類の安全性－設計のための一般原則－リスクアセスメント及びリスク低減）および JIS Z 8051（安全側面－規格への導入指針）に基づくリスクアセスメントの考え方を，機械ユーザーの作業段階にも適用したものである。さらに，無人航空機サービス事業者を対象とした規格である JIS Y 1011（ドローンサービスの品質−ドローンサービス事業者に対するプロセス要求事項）［17］では，サービス提供前のリスクアセスメントの実施が求められている。参考手法として SORA ガイドラインおよび JIS Z 8051 が併記され，SORA ガイドラインを推奨手法としている。このことから，無人航空機運用においては，運航と労働安全という異なる枠組みのリスクアセスメント手法が制度的に併存している状況にある。

既存研究においては，SORA ガイドラインまたは機械ユーザーのいずれか一方に基づくリスクアセスメントを扱った事例は存在するものの［5，18］，両手法を体系的に比較し，無人航空機運用に適用した研究は見当たらない。両手法の適用範囲や実施項目の差異を整理し，相互補完的な活用可能性を検討することは，無人航空機の安全運用において重要な課題である。SMS においても，航空安全と労働安全のマネジメントシステムの統合の検討が求められている。

本研究の目的は，無人航空機の社会実装において課題となる運航リスクと労働安全リスクを統合的

に扱う枠組みを整理・提案するものである。第 2 章では SORA ガイドラインおよび機械包括安全指針の概要を示す。第 3 章では両手法のリスクアセスメントを比較し，第 4 章では第 1 章 2 節で示すリサーチクエスチョンに基づいて考察を行う。第 5 章ではリスクアセスメント手法の統合的フレームワークを提案する。第 6 章で結論と今後の展望を述べる。

なお，本研究では，無人航空機の利用全体（飛行前後の準備作業，飛行，停止，保守等を含む）を指す用語として「運用」を用い，「運航」は無人航空機を飛行させる行為全般を指す場合に限定して用いる。

1-2　リサーチクエスチョン

本研究のリサーチクエスチョン（RQ）は以下のとおりである。

RQ1：SORA ガイドラインおよび機械包括安全指針が想定する無人航空機運用時のリスク領域は，どのような差異を有しているか

RQ2：両手法におけるリスクアセスメント実施項目には，どのような重複性および補完関係が存在するか

本研究では，これらのリサーチクエスチョンに対し，手法比較およびケーススタディに基づく考察を通じて検討を行う。

2. SORA ガイドラインと機械包括安全指針におけるリスクアセスメント手法の概要および適用結果

本章は，SORA ガイドラインと機械包括安全指針におけるリスクアセスメント手法の差異を明確化することを目的とする。まず両手法の一般的な構造や目的，実施項目を整理したのち，事例（ケース）に適用する。本章で対象とするリスクアセスメントは，主としてリスク評価までのプロセスとし，リスク低減措置にあたる，機械包括安全指針の「保護方策の実施」，SORA ガイドラインの「Step#6 リスク評価結果に対する対応」については，対象外とする。

2-1　ケースの概要

本研究では，両手法に適用する共通ケースとして，無人航空機を利用した建物外壁調査の実証試験を想定する：建物外壁に設置した複数のマーカーを無人航空機のカメラで撮影する運用を対象とし，飛行場所は福島ロボットテストフィールドの試験用プラント（高さ約 30 m）周辺を想定する*。

操縦者は建物から 30 m 以上離れた位置に配置され，一部は目視外飛行となる本ケースは飛行カテゴリー II に分類される。関係者は操縦者，試験スタッフ，見学者等の第三者とし，使用機体の仕様は代表的な市販小型マルチコプターの一般的仕様を参考に設定した。主な作業条件および機体仕様を**表 2.1** および**表 2.2** に示す。

表 2.1　作業条件

作業条件	飛行場所外観 福島ロボットテストフィールド HP より引用 [19]
場所：ロボットテストフィールド試験用プラント	
天候：晴れ	
作業目的：建物外周に設置された複数のマーカーの撮影	
気温：20 [℃]	
最大風速：5 [m/s]	
対象者：操縦者，試験スタッフ，見学者等（第三者）	
想定作業：事前準備，試験飛行，保守	
その他：一部目視外飛行，試験時の操縦は建物から 30 m 離れた位置	

* ここでのアセスメント結果は，論文中のアセスメント手法の説明の為の結果であり，実際の飛行に関するリスクアセスメントでは様々な要因が関係するため，結果が異なる可能性がある。

表 2.2　機体仕様抜粋

大きさ（L×W×H）	約 350×300×120［mm］
重量	約 1［kg］
最大飛行速度	約 20［m/s］
最大風圧抵抗	約 10［m/s］
最大飛行時間（無風時）	約 30［min］
最大伝送距離	約 5［km］

2-2　SORA ガイドラインの概要と適用結果

SORA ガイドラインは，無人航空機の飛行許可申請に用いられる国際的なリスクアセスメント手法である。本節では，SORA ガイドラインの構造および本ケースへの適用結果を整理する。

2-2-1　リスクの定義

SORA ガイドラインでは，リスクを「事象の発生確率とその重大性の組合せ」と定義する。

2-2-2　目的と適用範囲

SORA ガイドラインの目的はリスクアセスメントが必須となる飛行カテゴリー III 及び一部の飛行カテゴリー II の飛行許可申請を支援することである。また，飛行カテゴリー I についても適用可能である。評価対象は以下の 2 種類である。

- 地上リスク：無人航空機と人との衝突リスク
- 空中リスク：無人航空機と有人航空機との衝突リスク

無人航空機同士の空中衝突，無人航空機に搭載された貨物等による二次被害，プライバシーと財務に関わる事項については対象外である。

2-2-3　SORA ガイドラインにおけるリスクアセスメント手順の構造（Step#1〜Step#5）

SORA ガイドラインの実施手順を**図 2.1** に示す。本研究ではリスク評価を行う Step#5 までを対象とす

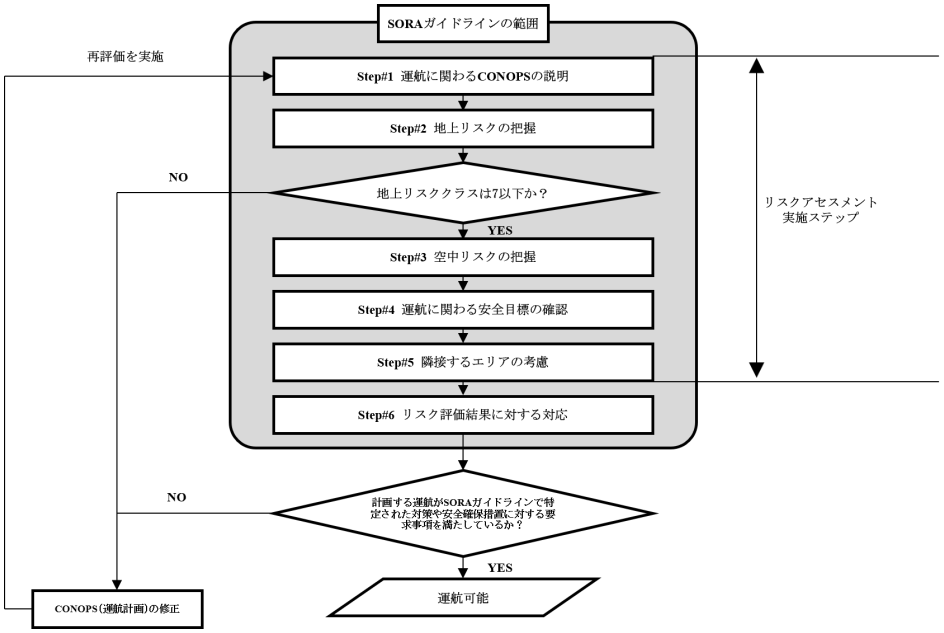

図 2.1　SORA ガイドラインの実施手順［12］

る。SORA ガイドラインの特徴は，リスク低減措置について「ロバスト性」を考慮する点にあり，ロバスト性は安全性の水準と保証の水準から構成される。ロバスト性は**表 2.3** により高～低レベルとなる。本研究ではリスク低減措置を扱わないが，Step#2，3 ではリスククラス調整に関してロバスト性が関係する。

表 2.3　ロバスト性レベルの決定［12］

		保障の水準		
		低	中	高
安全性の水準	低	低のロバスト性	低のロバスト性	低のロバスト性
	中	低のロバスト性	中のロバスト性	中のロバスト性
	高	低のロバスト性	中のロバスト性	高のロバスト性

【Step#1 運航に関わる CONOPS の説明】

無人航空機の運航内容を**表 2.1**，**2.2** 等の条件から CONOPS（Concept of Operations）として整理し，運航における 5W1H（When, Where, Who, What, Why, How）を明確化する。本研究では情報量が多いため詳細の記述は割愛する。

【Step#2 地上リスクの把握】

表 2.4，**表 2.5** に基づき，地上リスククラスの判定と調整を実施する。本ケースでは，最大飛行高度 30 m，低人口密度環境の目視外飛行とし，地上リスククラスは 3 と判定された。本ケースでは道路の通行者や他施設利用者の存在を考慮し，保守的に低人口密度環境として評価した。地上リスクの軽減策は以下 M1～3 の軽減策を実施し，地上リスククラスは 2 に調整された。

M1：飛行高度に対して 1：1 の水平距離を確保する。ロバスト性は低，調整数は -1。
M2：市販のパラシュートを搭載。ロバスト性は低，調整数は 0。
M3：飛行許可申請の審査要領に則った緊急対応策をとる。ロバスト性は中，調整数は 0。

表 2.4　地上リスククラスの判定表［12］（四角内文字は本稿でのアセスメント結果に対応）

地上リスククラス				
無人航空機の最大寸法	1 m	3 m	8 m	＞8 m
代表的な運動エネルギー見積	＜700 J	＜34 KJ	＜1084 KJ	＞1084 KJ
運航形態				
立入管理地域での目視内／目視外飛行※1	1	2	3	4
低人口密度環境での目視内飛行	2	3	4	5
低人口密度環境での目視外飛行※1	**3**	4	5	6
人口密集環境での目視内飛行	4	5	6	8
人口密集環境での目視外飛行※1	5	6	8	10
集会上空における目視内飛行	7	NA		
集会上空における目視外飛行※1	8			

※ 1　目視外飛行には補助者ありの目視外飛行も含む

表 2.5 地上リスクの軽減対策と地上リスククラスの調整数［12］（四角内文字は本稿でのアセスメント結果に対応）

軽減策の評価順	地上リスクの軽減策	ロバスト性		
		低／なし	中	高
1	M1–制御不能な状態となった際の無人航空機と衝突リスクに曝される人の数を減らす対策	0:なし※ **-1:低**	-2	-4
2	M2–有人航空機との衝突時のエネルギーを減らす対策	**0**	-1	-2
3	M3–制御不能となった際に被害の拡大を抑制するための緊急対応計画の設定	**1**	**0**	-1

※ M1 でロバスト性なしを選択できるのは，第 1 種機体認証を取得している機体に限る

【STEP#3 空中リスクの把握】

図 2.2 のフローチャートに従い，空中リスククラスを判定する。さらに，空中リスク低減には文献［12］に基づき次の「戦略的対策」と「戦術的対策」を適用する。

(1) 戦略的対策（任意）：有人航空機が運用されない時間帯・空域での運航調整
(2) 戦術的対策：目視または外部システム，検知システムによる衝突回避

「戦略的対策」を適用した後の残留空中リスククラスに対して，**表 2.6** に示す「戦術的対策」の性能要求レベルとロバスト性のレベルが必要となる。

本ケースでは，空中リスククラスは ARC-b となった。「戦略的対策」は適用せず，「戦術的対策」として，操縦者の死角となる領域に監視者を配置し，目視による衝突回避を採用した。

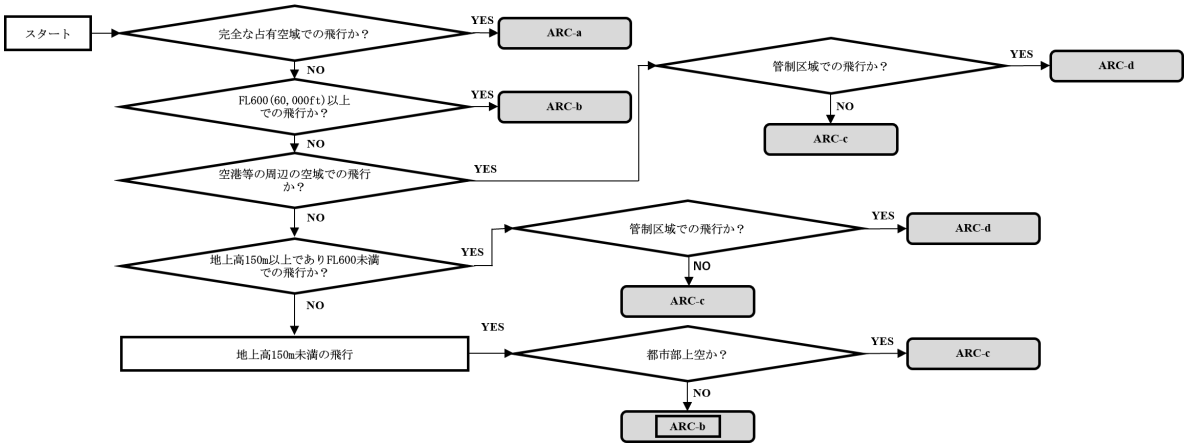

図 2.2 空中リスククラスの判定フローチャート［12］（四角内文字は本稿でのアセスメント結果に対応）

表 2.6 「戦術的対策」のレベルとロバスト性の割り当て［12］

残留空中リスククラス	「戦術的対策」の性能要求レベル	ロバスト性のレベル
ARC-d	高	高
ARC-c	中	中
ARC-b	低	低
ARC-a	要求なし	要求なし

【Step#4 運航に関わる安全目標（OSO：Operational Safety Objectives）の確認】

表 2.7 に基づき，安全性と保証のレベル（SAIL：Specific Assurance and Integrity Levels）と OSO の

ロバスト性を決定し，定められたリスク低減項目を実施することで許容可能なリスクを達成する。本研究では実質的なリスク評価である SAIL の決定までを取り扱う。 本ケースでは SAIL は II となった。

表 2.7　SAIL の決定［12］（四角内文字は本稿でのアセスメント結果に対応）

	最終的な空中リスククラス			
最終的な地上リスククラス	ARC-a	ARC-b	ARC-c	ARC-d
≦2	I	**II**	IV	VI
3	II	II	IV	VI
4	III	III	IV	VI
5	IV	IV	IV	VI
6	V	V	V	VI
7	VI	VI	VI	VI
>7	リスク評価対象外			

【Step#5 隣接するエリアの考慮】

無人航空機がエリアを逸脱した場合を考慮し，隣接するエリアの地上リスク・空中リスクの変動を評価する。本ケースでは隣接エリアとして試験用プラントが設置されている福島ロボットテストフィールド全域を想定した。この場合，隣接エリアでも大きなリスク変動は見られず，追加の対策は不要と判断した。

2-3　機械包括安全指針の概要と適用結果

機械包括安全指針は，機械の設計段階および使用段階における労働者の安全確保のためのリスクアセスメント指針である。本節ではその構造および本ケースへの適用結果を整理する。

2-3-1　リスクの定義

リスクを「負傷または疾病の重篤度と，その発生可能性の度合い」と定義する。

2-3-2　目的と適用範囲

機械包括安全指針の目的は，機械の設計・製造段階および使用段階における安全化を図り，労働災害を防止することである。適用範囲は，労働において使用されるすべての機械と，それに付随する準備・保守作業を含む全ての作業である。

2-3-3　実施項目（ユーザー側①〜④）

図 2.3 に機械包括安全指針の実施項目を示す。本研究ではユーザー側のリスクアセスメント項目①〜④を対象とし，本ケースのリスクアセスメントツールは文献［5］のツールを使用した。

【①情報の入手】

使用する機械と作業の前提条件及び，メーカーが機械を設計した後のリスク（残留リスク）についての情報を明確にすることが求められる。本研究では，情報量が多いため，Step#1 と同様に割愛する。

【②危険性または有害性の同定】

収集した情報をもとに，作業における災害を起こす根源（危険源）と，事故を起こしえる現象（危険事象）を導出する。

本ケースでは，危険源が多数存在するため代表的なものを抜粋した。無人航空機本体だけでなく，破損したプロペラやバッテリーなどの無人航空機の部品や構造物も危険源となり得る。

【③リスク見積等】

マトリクス法，加算法などのツールを用いてリスクを見積もる。無人航空機は広範囲に移動し，対

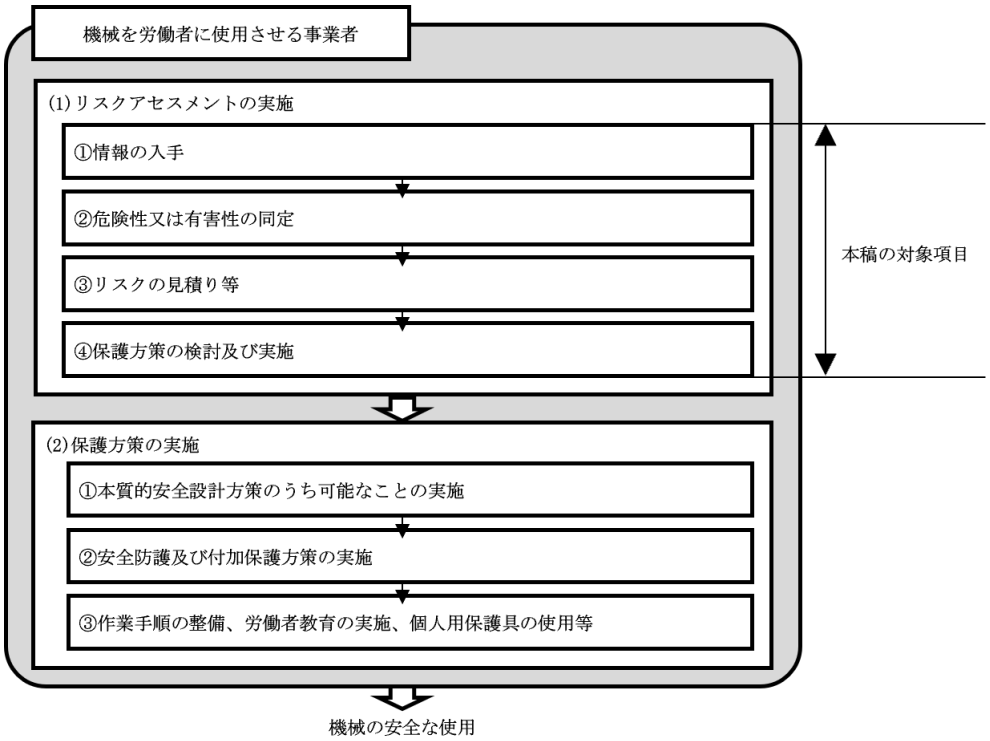

図 2.3　機械包括安全指針に基づく機械の安全化の手順（文献［16］別図から抜粋，加工して作成）

象者ごとに危険事象が変化するため，同一危険源でも複数のリスクが発生する。本ケースでは導出されたリスクは 100 を超えた。リスク要素の評価は文献［5］を参考に**表 2.8** および**表 2.9** に基づいて行った。

表 2.8　リスク要素の点数化

危害の酷さ S		危険事象の発生確率 Ps		暴露頻度 F		回避される可能性 A	
危害の程度	点数	発生確率	点数	頻度	点数	回避可能性	点数
致命傷	10	確実	6	頻繁	4	不可避	4
重傷	6	可能性が高い	4	時々	3	稀に回避	3
中傷	4	可能性がある	3	たまにある	2	時々回避	2
軽傷	3	可能性が低い	2	ほとんどない	1	ほとんど回避	1
掠り傷程度	2	ほとんどない	1				
軽微な損害	1						

表 2.9　リスク見積と判定基準

リスク見積／評価基準	内容
算出表	リスク点数（R）＝危害の酷さ（S）×危害の発生確率（Ph）
危害の発生確率	危害の発生確率（Ph）＝暴露頻度（F）＋発生確率（Ps）＋回避可能性（A）
判定基準	3＜R＜6　十分低い／無視できる 7＜R＜14　低い／条件付き受容 15＜R＜50　中程度／検討を要する 51＜R＜140　高い／受容できない

【④保護方策の検討及び実施】

表 2.9 の判定基準を用いて低減の必要性を判断する。本ケースでは 100 を超えるリスクが導出され，本章では代表例のみを**表 2.10** に示す。灰色部分は「高い／受容できない」と評価されたリスクである。

表 2.10　機械包括安全指針によるリスクアセスメント実施結果代表例

危険源同定							リスク見積					
段階	No.	危険源	危険状態/危険事象	想定危害	対象者	危害の酷さS	危害の発生確率 Ph				リスク点数R
								頻度F	確率Ps	回避A	
事前準備	1	無人航空機本体の落下	無人航空機を調整の為低空で飛行させた際に無人航空機が落下し試験スタッフに衝突し、裂傷する	墜落	試験スタッフ	3	9	3	3	3	27
	2	プロペラの衝突	無人航空機を調整の為低空で飛行させた際に無人航空機が試験スタッフに衝突してプロペラが目にあたり、失明する	衝突	試験スタッフ	6	7	3	3	1	42
	3	外れたプロペラの衝突	調整飛行中にプロペラが外れて試験スタッフの目にあたり、失明する	衝突	試験スタッフ	6	9	3	2	4	54
	4	破損したプロペラの衝突	調整飛行中にプロペラが構造物にあたり、破損して破片が周囲に飛び、試験スタッフの目にあたり、失明する	衝突	試験スタッフ	6	10	3	3	4	60
	5	バッテリーの発火	無人航空機の調整飛行中にバッテリーに負荷がかかって発火し、試験スタッフがやけどを負う	火災	試験スタッフ	3	6	2	2	2	18
飛行	6	操縦ミスによる無人航空機本体の落下	無人航空機を飛行させた際に操縦ミスにより無人航空機が構造物に接触・落下して見学者等に衝突し、頸椎骨折する	衝突	見学者等	10	7	2	2	3	70
	7	操縦ミスによる無人航空機本体の落下	無人航空機を飛行させた際に操縦ミスにより無人航空機が構造物に接触・落下して試験スタッフに衝突し、頸椎骨折する	衝突	試験スタッフ	10	8	3	2	3	80
	8	情報伝達ミスによるプロペラとの衝突	試験スタッフが無人航空機に触れていることに気づかずに離陸操作をしてしまい、プロペラが試験スタッフの目にあたり、失明する	失明	試験スタッフ	6	8	2	2	4	48
保守	9	バッテリ充電部での感電	試験スタッフがバッテリー交換時に濡れた手で充電端子間に触れて感電する	感電	試験スタッフ	3	8	2	2	4	24
	10	バッテリーの発火	充電している予備バッテリーが発火して周囲の可燃物が延焼し、作業スタッフが火傷を負う	火傷	作業スタッフ	3	6	2	2	2	18

3. SORA ガイドラインと機械包括安全指針のリスクアセスメント手法の比較

両手法を共通ケースに適用した前章の結果をもとに，本章では，リスクの定義，目的と適用範囲，リスクアセスメント実施項目，リスクアセスメント実施例を順に比較検討し，両手法の対応関係と相違点を明らかにする。

3-1　リスクの定義の比較

リスクアセスメント手法を比較するにあたり，それぞれが対象とするリスクの定義を確認する必要がある。両手法はいずれもリスクを「発生可能性（確率）と危害の重大性の組合せ」と捉えており，評価の考え方（リスクは低いほど望ましい）も一致する。したがって，本章では定義差による解釈の齟齬は小さいものとして，手順・適用範囲の差異に焦点を当てて比較する。

3-2　目的と適用範囲の比較

SORA ガイドラインの主目的は，飛行許可申請を支援することである。このため，危害の対象となるのは，第三者や有人航空機（正確にはその搭乗者）であり，危険源は無人航空機本体に限定されていると考えられる。一方，機械包括安全指針の目的は，機械の使用に伴う労働災害の防止であり，危険源は無人航空機本体だけでなく，構成部品や周辺構造物にまで及ぶ。また考慮する作業は運航に加え事前準備や保守などの運用に関わる全ての作業である。

JIS B 9700 における機械の定義は，「連結された部品またはコンポーネントのうち，少なくとも一つが特定の目的のために稼働し，協働するもの」であり，無人航空機はこの定義に該当する。したがって，無人航空機運用は機械包括安全指針の適用範囲内であると考えられる。

3-3　リスクアセスメント実施項目の比較

SORA ガイドラインと機械包括安全指針のリスクアセスメント実施項目を比較し，**表 3.1** に関係対応表として整理した。縦軸に機械包括安全指針，横軸に SORA ガイドラインのリスクアセスメント実施項目を配置し，実施内容に関係あるものを「○」，ある程度関係のあるものを「▲」，該当のないものを灰色で示した。以下 (1) ～ (4) に SORA ガイドラインと機械包括安全指針を比較した結果を示す。

表 3.1 SORA ガイドラインと機械包括安全指針の実施項目比較

				SORAガイドライン													
				Step#1 運航に関わるCONOPSの説明							Step#2 地上リスクの把握		STEP#3 空中リスクの把握			Step#4 運航に 関わる 安全目標 の確認	Step#5 隣接するエリアの考慮
○：関係あり ▲：ある程度関係あり				Why ・運航目的	When ・運航日時	Where ・運航地域／空域	How ・運航	Who ・運航組織の概要 ・訓練	What ・使用する無人航空機について	How ・操縦システムについて	地上リスククラスの判定	地上リスククラスの低減	空中リスククラスの判定	「戦略的対策」を適用した空中リスククラスの低減	「戦術的対策」による空中リスクの軽減及び要求レベル	安全性と保証のレベル(SAIL)の決定	
機械包括安全指針	情報の入手	作業標準、作業手順書		○	○	○	○	○	○								
		機械設備等のレイアウト、作業周辺の環境に関わる情報				○	○										○
		複数の事業者が同一の作業で作業を実施する状況に関する情報						○									
		使用上の情報	製造等を行う者の名称及び住所						○								
			型式又は製造番号等の機械を特定するための情報						○								
			機械の仕様及び構造に関する情報						○	○							
			機械の使用等に関する情報 -意図する使用の目的及び方法 -運搬、設置、試運転等の使用の開始に関する情報 -解体、廃棄等の使用の停止に関する情報 -機械の故障、異常等に関する情報 -合理的に予見可能な誤使用及び禁止する使用方法						○	○							
			安全防護及び付加保護方策に関する情報						○	○							
			機械の残留リスク等に関する情報						○	○							
		その他、調査等の実施に当たり参考となる資料等						○	○	○							
		製造者、管理権原を有する者，元方事業者のリスクアセスメント情報入手					○		○								
		災害事例、災害統計等															
	危険性又は有害性の同定	機械に労働者が関わる作業等における危険性又は有害性の同定を行う	機械の意図する使用が行われる作業								▲		▲				
			機械に故障、異常等が発生している状況における作業								▲		▲				
			機械の合理的に予見可能な誤使用が行われる作業								▲		▲				
			機械を使用する労働者以外の者（合理的に予見可能な場合に限る。）が機械の危険性又は有害性に接近すること								▲		▲				
			運搬、設置、試運転等の機械の使用の開始に関する作業														
			解体、廃棄等の機械の使用の停止に関する作業														
	リスクの見積り等	リスクを見積もり，リスクの低減の優先度を検討する									○		○			○	○
	保護方策の検討及び実施	適切なリスクの低減が達成されているかどうか判定する														○	

(1) 機械包括安全指針「情報の入手」と SORA ガイドラインとの関係

「情報の入手」は，機械の仕様，作業内容，作業対象者を明らかにする項目である。したがって，「情報の入手」は SORA ガイドラインの Step#1 に対応するだけでなく，運用区域・隣接区域の条件を精査する Step#5 とも一部対応すると整理できる。

機械包括安全指針では災害事例・災害統計等をリスクアセスメント実施者が入手することを求めている。一方，航空業界では災害事例・統計が ICAO Annex 13 [20] 等に基づき収集・分析が適時行われ，必要に応じてサーキュラ等で基準変更が通達されるため，SORA ではリスクアセスメント実施者に個別に災害事例・災害統計等を入手することは求めていないと考えられる。

(2) 機械包括安全指針「危険性または有害性の同定」と SORA ガイドラインとの関係

危険源および危険事象を導出する機械包括安全指針の項目は，SORA ガイドラインの Step#2・Step#3 と部分的に対応する。ただし，SORA ガイドラインの地上リスク・空中リスクは無人航空機の運航（飛行中）に限定されるため，「運搬・設置・試運転」や「解体・廃棄」など運航の前後に関わる項目には対応しない。

(3) リスクアセスメント中のリスク低減（SORA ガイドライン特有の項目）

SORA ガイドラインの Step#2「地上リスククラスの低減」，Step#3「戦略的対策の適用」「戦術的対策による空中リスクの軽減」は，リスクアセスメント中にリスクを低減する手順であり，機械包括安全指針はリスクアセスメント後にリスク低減を実施するため，該当する項目が存在しない。

(4)　リスクの見積と両手法の対応

機械包括安全指針の「リスクの見積等」は，リスクを明らかにする項目であり，地上リスクと空中リスクを明らかにする Step#2，3，SAIL を明らかにする Step#4，近接エリアのリスクを明らかにする Step#5 を関係ありとした。

3-4　SORA ガイドラインと機械包括安全指針のリスクアセスメント実施例の比較

以下では，前章で示した共通ケースの適用結果に基づき，SORA ガイドラインと機械包括安全指針におけるリスクアセスメント実施結果の特徴的な差異を比較する。

(1)　無人航空機と人との衝突リスクの違い

SORA ガイドラインでは，無人航空機と人との衝突リスクである地上リスククラスは 1 つの値として導出される。一方，機械包括安全指針では**表 2.10** の No.1，2，6，7，8 に示すように，複数のリスクとして導出される。これは，危険事象が対象者や状況により異なるためである。例えば，撮影対象の建物周辺には試験スタッフだけでなく見学者等が存在する可能性があり，実施作業や場所が変わるため，No.6 と No.7 のように別リスクとして扱われる。逆に，無人航空機が自動離発着し周囲に作業者が存在しない環境では，両手法の危険事象を一致させることが可能と考えられる。

また，本ケースの地上リスククラスは最大 8 に対して 2 であるため，機械包括安全指針におけるリスク尺度に基づく評価と比較すると，相対的に低リスクと受け取られる可能性がある。これは，両手法におけるリスク評価の目的および評価視点の相違に起因する：SORA ガイドラインは，**表 2.7** に示される無人航空機業界全体の SAIL の枠組みに基づき，対象とする運航リスクが業界全体のどの水準に位置付けられるかを相対的に評価し，当該運航に対する飛行申請が業界全体として合理的であるかを判断することを目的としている。これに対し，機械包括安全指針は，個々の作業単位に着目してリスクを評価し，そのリスクの受容可能性を判断するための手法である。このように，両手法のリスク見積は目的が異なるため，数値の解釈および比較にあたっては注意が必要である。

(2)　無人航空機と有人航空機の衝突リスク

SORA ガイドラインでは，無人航空機と有人航空機の衝突リスクである空中リスククラスは 1 つの値として導出される。一方，機械包括安全指針ではこの衝突リスクは導出されなかった。これは，本ケースの無人航空機の最大高度が建物と同程度であり，有人航空機の高度帯と重ならないためである。機械包括安全指針の「合理的に予見可能な誤使用」として無人航空機の最大高度の変更がどの程度考慮されるべきかは，今後検討が必要と考えられる。

SORA ガイドラインにおいてこのリスクが必ず評価されるのは，飛行許可申請において「有人航空機への影響」は極めて重大な情報であるためと考えられる。

(3)　無人航空機の運航以外のリスクの違い

SORA ガイドラインは，運航中の無人航空機に着目していると考えられるため，事前準備・保守作業のような飛行以外の作業や，バッテリー火災，破損プロペラのような無人航空機本体以外による負傷などは対象外である。一方，機械包括安全指針ではこれらもリスクアセスメントの対象として扱われ，より広範なリスクが導出される。

(4)　リスク数値の変動性の違い

SORA ガイドラインは，表やフローチャートによりリスクが決定されるため，リスクアセスメント実施者によるリスク見積の差は生じにくい。一方，機械包括安全指針はリスク要素の判断に定性的な部分を多く含むため，リスクアセスメント実施者によるリスク見積の変動が大きくなる可能性が高い。この点は，両手法の評価特性の違いとして留意すべき事項である。

以上から，両手法は「無人航空機本体を危険源とする点」では重複する一方，「運航中心か／作業全体か」という観点で適用範囲が異なる。したがって，無人航空機運用におけるリスクの見落としを抑制するためには，両手法の評価結果を相互に参照しつつ，体系的に統合して適用する枠組みが必要であると考えられる。

4. リサーチクエスチョンに対する考察

前章では，SORA ガイドラインと機械包括安全指針について，共通ケースへの適用結果を基に，リスクアセスメント手法の構造および実施項目の差異を比較した。本章では，その比較結果を踏まえ，本研究で設定したリサーチクエスチョン（RQ1，RQ2）に対する考察を行う。

4-1 SORA ガイドラインおよび機械包括安全指針が想定する無人航空機運用時のリスク領域の差異（RQ1）

本節では，適用範囲および実施項目の比較，さらにリスクアセスメント実施例に基づき，SORA ガイドラインと機械包括安全指針が対応するリスク領域の構造的差異について考察する。

本研究では，無人航空機運用におけるリスクを，「空中リスク（AR）」，「地上リスク（GR）」および「その他のリスク（OR）」から構成されるものと定義し，これを UR と表記する。GR はさらに，無人航空機と第三者との衝突リスク（GRO）と無人航空機と作業者の衝突リスク（GRW）から構成される。SORA ガイドラインおよび機械包括安全指針におけるリスクの領域は，**図 4.1** に示すように概念的に整理することができる。横軸は無人航空機運用におけるリスクの領域，縦軸は作業フェーズを表す。

図 4.1 に示す横軸の点線矢印部分は，両手法が想定する前提条件の違いにより，対象とするリスクの領域が各手法の想定と一致しない可能性のある範囲を示している。

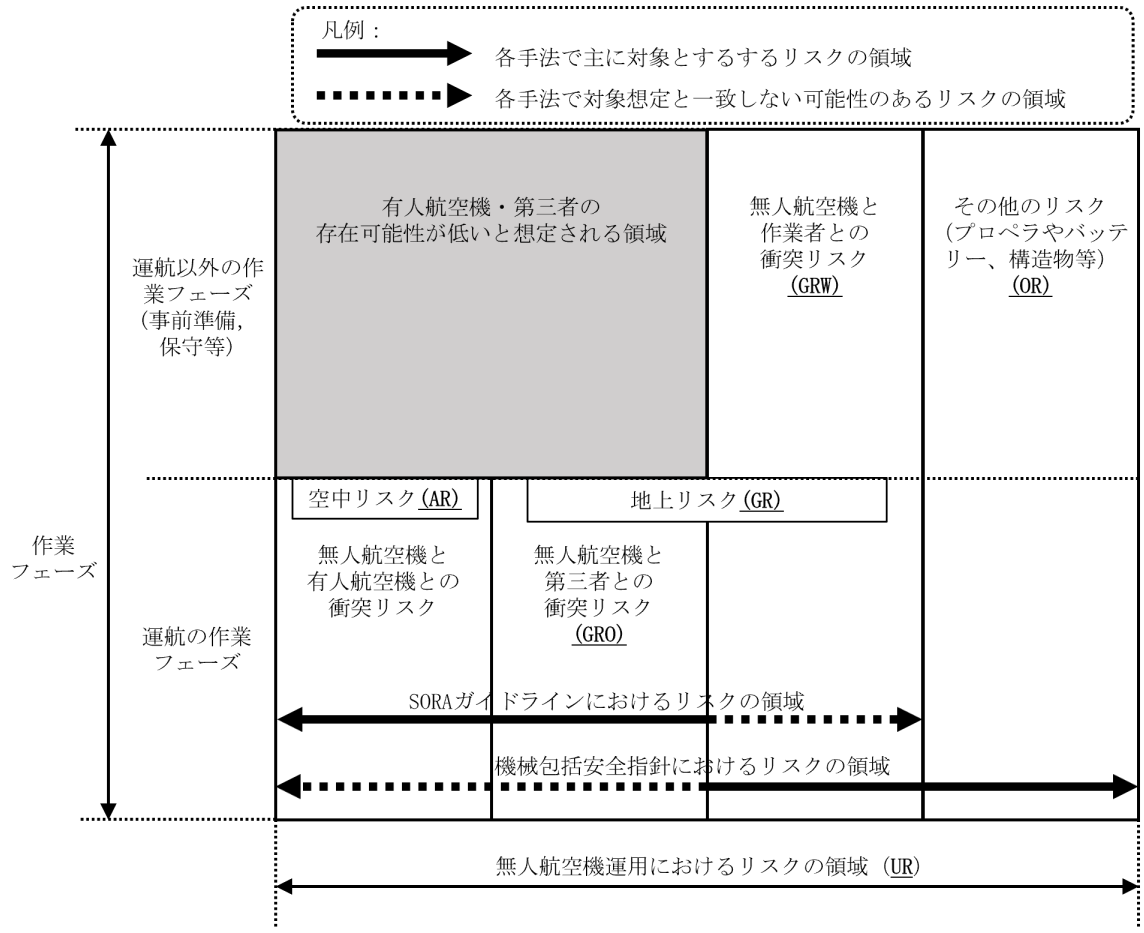

図 4.1 SORA ガイドラインと機械包括安全指針の対応リスクの範囲

SORA ガイドラインでは，「無人航空機と第三者」および「無人航空機と有人航空機」の組合せに着目しており，これは飛行許可申請において周囲への影響を説明する必要があるためであると考えられる。一方，機械包括安全指針は労働者の安全を目的として，作業に関わるすべての危険源と作業者との組合せを対象とするため，対応するリスク領域は相対的に広くなる。

図中の灰色領域は，運航以外の作業フェーズにおいて，有人航空機や第三者の存在可能性が低いと想定される領域を示している。ただし，これらの存在が合理的に予見可能な場合には，機械包括安全指針の手法によりリスクを導出し，評価することが可能である。

リスクアセスメント実施例からも示されたように，機械包括安全指針では危険事象を細分化し，リスクを個別に導出する。このためリスク数は多くなるが，原因に応じた具体的なリスク低減方策を検討することが可能である。一方，SORA ガイドラインでは危険事象を個別に扱わないが，地上リスクおよび空中リスクに応じてあらかじめ定められたリスク低減方策を適用することで，実質的に機械包括安全指針の細分化された危険事象への対応を包含している可能性がある。

以上のことから，SORA ガイドラインと機械包括安全指針が主として対応するリスク領域は必ずしも一致しておらず，両手法の適用範囲には明確な違いがある。したがって，両手法を組み合わせて適用することで，無人航空機運用においてより広範なリスクに対応できると考えられる。

4-2　両手法におけるリスクアセスメント実施項目の重複性および補完関係（RQ2）

表 3.1 およびリスクアセスメント実施例から，SORA ガイドラインは使用する無人航空機本体に関する情報と，運航に関わる情報を明確に整理する手法であるため，機械包括安全指針の複数の項目と重複する部分が存在する。特に，機械包括安全指針における「情報の入手」および「危険性または有害性の同定」に対応する要素は，SORA ガイドラインの Step#1～Step#3 の内容と重なる部分が多い。しかし，SORA ガイドラインは運航中の無人航空機を主たる評価対象とするため，作業者に関する情報や，無人航空機の運用における「使用の開始」や「使用の停止」に該当する作業（離発着準備，機体の設置・撤去，保守・点検作業など）に関する情報は十分に扱われていない。これらは機械包括安全指針ではリスクアセスメントの重要な対象として位置付けられている。

したがって，無人航空機運用におけるリスクアセスメントを実施する際には，SORA ガイドラインで扱われる無人航空機運航時のリスクに加え，機械包括安全指針で扱われる作業者情報や運用準備・停止作業に関するリスクを補完的に明確化する必要があると考えられる。

機械包括安全指針の「情報の入手-災害事例，災害統計等」と SORA ガイドラインの「Step#2-地上リスククラスの低減」，「Step#3-戦略的対策を適用した空中リスククラスの低減，戦術的対策による空中リスクの軽減及び要求レベル」は各手法独自の項目になるが，実施結果はリスクを導出する過程で重要な情報となるため，実施順序を考慮し，両手法で取り入れることが適切なリスク評価に有効であると考えられる。

4-3　リサーチクエスチョンに対する考察のまとめ

以上の考察結果から，両手法が想定するリスク領域および実施項目には明確な構造的差異と補完関係が存在することが示された。次章では，これらの結果を踏まえ，RQ1 および RQ2 で得られた知見に基づき，SORA ガイドラインと機械包括安全指針を統合的に活用するためのリスクアセスメント手法の統合的フレームワークを提案する。

5. リスクアセスメント手法の統合的フレームワークの提案

前章では，SORA ガイドラインおよび機械包括安全指針が想定する無人航空機運用時のリスク領域の構造的差異，ならびにリスクアセスメント実施項目の重複性および補完関係を明らかにした。

本章では，これらの知見に基づき，両手法の特性を相互補完的に活用するリスクアセスメントの統合的フレームワークを提案する。

RQ1 が示したように，SORA ガイドラインは運航の作業フェーズの地上・空中リスクの評価に強み

を持つ一方，機械包括安全指針は運航以外の作業フェーズ，作業者を含むより広範なリスクに対応できる。

RQ2 の結果からは，両手法に共通する項目と相互に補完すべき項目が明確化された。

提案するフレームワーク（**図 5.1**）は，図中に示す①～④の手順に従ってリスクアセスメントを実施し，SORA ガイドラインに基づくリスクアセスメントの情報を機械包括安全指針に基づくリスクアセスメントへ段階的に反映させることを特徴としている。この手順に則ることで，両手法に共通する項目を効率的に統合するとともに，それぞれの手法が得意とする領域を活かし，リスクの見落としを抑制するリスクアセスメントを実現する構造を有している。

以下に，本フレームワークの適用例に基づきその詳細を説明する。SORA ガイドラインにおけるリスクアセスメントの情報は，**図 5.1** の「使用する無人航空機の情報」および「運航の作業に関わる情報」へ反映される構造となっている。図中の黒色矢印は情報が大部分の反映，点線矢印部分は一部の反映が可能であると考えられることを示している。特に，「使用する無人航空機の情報」については，機械包括安全指針におけるリスクアセスメントでは詳細な整理が示されていないため，SORA ガイドラインにおけるリスクアセスメントの情報は有用であると考えられる。

また，SORA ガイドラインの Step#2 および Step#3 におけるリスククラス低減方策の情報も，機械包括安全指針におけるリスクアセスメントに影響を与える。例えば，SORA ガイドライン Step#2 の地上リスククラス低減項目で，「M2：無人航空機との衝突時のエネルギーを減らす手段」として無人航空機にパラシュートの搭載を選択した場合，「使用する無人航空機の情報」に反映され，作業者のリスク見積にも波及する。これは，パラシュートの搭載が第三者との衝突時だけでなく，作業者との衝突時においても危害の低減効果を有すると考えられるためである。具体的には，**表 2.10** の No.7 は，リスク低減方策がとられていない状態のリスクであるが，パラシュートの搭載というリスク低減方策を前提条件とする場合，危害の酷さ S の低減が期待できる。リスク低減措置の効果を考慮し，**表 2.10** の No.7 について再見積を行い，危害の酷さ S が 10 から 4 に低減すると評価される場合，リスクの数値は 80 から 32 に低減される。同様に，空中リスクに対する戦術的対策として監視者配置を選択した場合，情報は機械包括安全指針における作業体制や人的配置に関するリスク見積にも反映される。

一方で，SORA ガイドラインのリスク低減方策を前提条件として導入する場合，当該方策が新たな

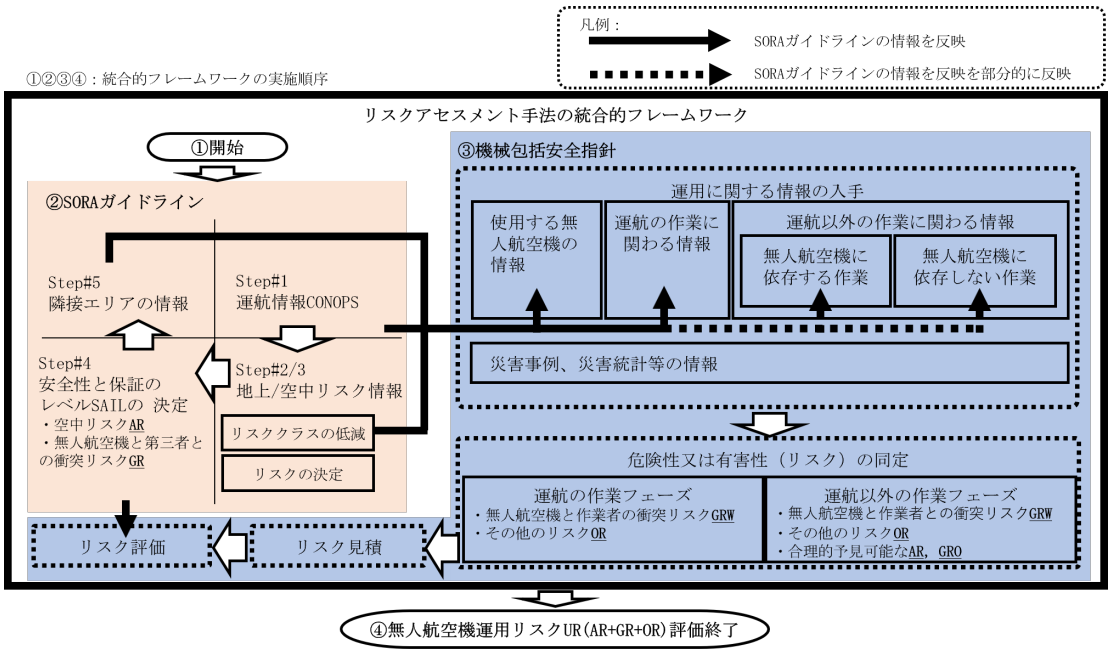

図 5.1　無人航空機運用におけるリスクアセスメント手法の統合的フレームワーク

危険源や危険事象を生じさせないかについても検討が必要である。例えば，パラシュートの搭載は墜落時の衝突エネルギーを低減できる一方で，墜落範囲の拡大により衝突対象となる第三者が増加するおそれや，パラシュート展開時に建物等の構造物へ引っ掛かりやすくなること，さらに回収作業時における作業者のリスクが増加することなどが合理的に予見される。このような場合には，本フレームワークに基づき，前提条件の変化を**図 5.1**③内の「運用に関する情報の入手」に反映することで，合理的予見可能なリスクとして導出することができると考えられる。

このように，SORA ガイドラインのリスクアセスメント情報は，機械包括安全指針におけるリスクアセスメントの対象となるリスク領域（GRW 及び OR）のリスク見積・評価に有用であるとともに，無人航空機運用事業者や安全管理者がリスクアセスメントを実施する際の情報整理の負担軽減にも寄与すると考えられる。

本研究で提案したフレームワークは，飛行許可申請において必要となる情報と，現場における無人航空機運用時の労働安全リスク評価を，同一の検討プロセス上で整理できる点に特徴がある。これにより，事業者や安全管理者は，複数の制度や指針を個別に解釈する負担を軽減しつつ，実務に即した安全運用方法の検討が可能となる。また，労働安全分野におけるリスクアセスメントの実務者は多く，そうした人材の知見や経験を無人航空機運用のリスクアセスメントに活用できる点も，本フレームワークの利点の一つであると考えられる。

6. お　わ　り　に

本研究では，無人航空機運用におけるリスクアセスメント手法の課題を明らかにするため，SORA ガイドラインおよび機械包括安全指針の比較分析を行い，リサーチクエスチョン（RQ1，RQ2）に対する検討を実施した。RQ1 では，両手法によって対応し得るリスク領域を整理した結果，**図 4.1** に示すように，両者が対象とする範囲には相違があり，両者を相補的に用いる必要性が示された。RQ2 では，両手法のリスクアセスメント実施項目を比較した結果，無人航空機飛行時のリスクに関する情報は両手法で共通している一方，作業者情報や運用準備・停止作業といった，飛行時以外の無人航空機運用に特有のリスクは機械包括安全指針側で補完的に扱う必要があり，SORA のみでは十分に評価されない領域が存在することが確認された。

以上の RQ1，RQ2 の考察結果を踏まえ，本研究で提案したフレームワークでは，飛行許可申請に用いられる SORA ガイドラインを先行して実施し，その結果を機械包括安全指針に基づく評価へ段階的に反映する手順とした。このフレームワークを用いることで，飛行許可申請に必要な情報整理と現場における無人航空機運用時のリスク評価を，同一の検討プロセス上で整理できるようになった。

本研究で提案したフレームワークにより，無人航空機運用に関わる事業者や安全管理者は，複数の制度や指針を個別に解釈する負担を軽減しつつ，実務に即したリスクアセスメントを実施できると期待される。また，労働安全分野で蓄積されてきたリスクアセスメントの知見や人材を無人航空機運用に活用できる点も，本フレームワークの利点である。

本研究の今後の展望として次が考えられる：本研究ではリスク評価までを主対象とし，リスク低減プロセスそのものは扱っていない。SORA ガイドラインにおけるリスク低減策は，ロバスト性の概念を用いて対策の水準を評価する点に特徴を有している。一方，機械包括安全指針は，「本質的安全設計方策」「安全防護及び付加保護方策」「作業手順書，教育，保護具の着用（人による対策）」の順にリスク低減を進める点に特徴がある。両手法は，それぞれ航空機運航および労働安全の分野で蓄積された知見に基づく手法であることから，今後は，本研究で示した統合的フレームワークを基盤として，両手法のリスク低減方策の関係性を明確にし，それぞれの特徴を組み合わせることにより，無人航空機運用におけるより効率的かつ実践的なリスク低減手法へ発展させることに取り組んでいきたい。

謝　　辞

この成果は，NEDO（国立研究開発法人新エネルギー・産業技術総合開発機構）の委託業務（JPNP22002）の結果得られたものです。

投稿受付：2026 年 1 月 9 日
採録決定：2026 年 2 月 13 日

文　　献

［1］ K. Nonami, F. Kendoul, S. Suzuki, W. Wang, and D. Nakazawa：“Autonomous Flying Robots: Unmanned Aerial Vehicles and Micro Aerial Vehicles”, Springer, 2010.
［2］ 久保 大輔：“無人航空機システム（ドローン）の歴史と技術発展”，計測と制御，Vol.56, No.1, pp12–17, 2017.
［3］ 小型無人機に関する関係府省庁連絡会議：“空の産業革命に向けたロードマップ～小型無人機の安全な利活用のための技術開発と環境整備～”，［Online］. Available: https://www.kantei.go.jp/jp/singi/kogatamujinki/pdf/siryou7.pdf
［4］ 小型無人機に関する関係府省庁連絡会議：“空の産業革命に向けたロードマップ 2024”，［Online］. Available: https://www.kantei.go.jp/jp/singi/kogatamujinki/pdf/roadmap2024.pdf
［5］ 岩田 拡也，加藤 晋：“無人航空機（ドローン）の歴史と安全―社会が受容可能なリスクとベネフィットのバランス―”，安全工学，Vol.55, No.4, pp237–243, 2016.
［6］ 国土交通省：“無人航空機の事故及び重大インシデントの報告要領”，［Online］. Available: https://www.mlit.go.jp/koku/content/001520661.pdf
［7］ 五十嵐 広希：“国内における無人航空機の重大事故事例報告”，信頼性・保全性・安全性シンポジウム，第 51 回 8-1，2022.
［8］ 国土交通省：“無人航空機に係る事故等報告一覧”，［Online］. Available: https://www.mlit.go.jp/common/001585162.pdf
［9］ 国土交通省：“令和 5 年度　事故等統計情報”，［Online］. Available: https://www.mlit.go.jp/koku/content/001747880.pdf
［10］ 国土交通省：“無人航空機（ドローン，ラジコン機等）の安全な飛行のためのガイドライン”，［Online］. Available: https://www.mlit.go.jp/common/001303818.pdf
［11］ 国土交通省：“無人航空機の飛行に関する許可・承認の審査要領（カテゴリー III 飛行）”，［Online］. Available: https://www.mlit.go.jp/common/001586101.pdf
［12］ 福島ロボットテストフィールド：“安全確保措置検討のための無人航空機の運航リスク評価ガイドライン”，2023，https://www.fipo.or.jp/robot/initiatives/guidelines（accessed Dec.17, 2025）.
［13］ 国土交通省：“無人航空機の飛行の安全に関する教則”，［Online］. Available: https://www.mlit.go.jp/koku/content/001860311.pdf
［14］ JARUS：“JARUS guidelines on Specific Operations Risk Assessment（SORA），JAR-DEL-SRM-SORA-MB-2.5”，［Online］. Available: http://jarus-rpas.org/wp-content/uploads/2024/06/SORA-v2.5-Main-Body-Release-JAR_doc_25.pdf
［15］ ICAO：“Doc 9859 Safety Management Manual, Fourth Edition”, 2018
［16］ 厚生労働省：“「機械の包括的な安全基準に関する指針」の改正について”，2007，基発第 0731001 号.
［17］ JIS Y 1011：“ドローンサービスの品質－ドローンサービス事業者に対するプロセス要求事項”，2024.
［18］ 中村 裕子，坂本 修，佐藤 一郎，中島 徳顕，髙田 淳，石井 啓吾，田中 秀治，久根﨑 将人：“無人航空機運航リスクアセスメント手法 SORA 国内実証実験への適用～ケーススタディ：新上五島町での無人ヘリコプター物流～”，次世代移動体技術誌，Vol.2, No.4, PP42-55, 2021.
［19］ 福島ロボットテストフィールド：“インフラ点検・災害対応エリア - 試験用プラント”，https://rtf.f-rei.go.jp/facility-use/considering-use/facility/infrastrucrure（accessed Dec.17, 2025）.
［20］ ICAO：“Annex 13 to the Convention on International Civil Aviation — Aircraft Accident and Incident Investigation, Thirteenth Edition”, 2024

蓮實　雄大
職業能力開発総合大学校安全ユニット助教。労働安全に関する研究に従事。長岡技術科学大学大学院経営研究科システム安全専攻修了。長岡技術科学大学，会津大学研究員を経て，2020 年より現在に至る。
E-mail: y-hasumi@uitec.ac.jp

中村　瑞穂
職業能力開発総合大学校安全ユニット教授。職業訓練指導員の養成，再訓練，基盤整備事業に従事している。主に機械安全・労働安全・安全管理に関する研究・教育訓練を担当している。博士（工学）。
E-mail: nakamura@uitec.ac.jp

北條理恵子
長岡技術科学大学システム安全専攻准教授。働く人の目線からの安全制御システムの有効性評価，適切な作業行動のための行動分析学的介入，働く人のウェルビーイング評価，働く人が行うリスクアセスメント施行に関する手法開発に関わる研究に従事。博士（獣医）。
E-mail: r_hojo@vos.nagaokaut.ac.jp

是村　由佳
コレムラ技研バラスト事業部運営責任。人と組織のコンサルタント。産業安全行動分析学研究会（日本機械学会，産業・化学機械と安全部門）。2001 年北テキサス大学行動分析学修士，2008 年同大学学際領域情報科学博士。慶應義塾大学助教を経て 2010 年より現在に至る。
E-mail: yuka@ballast.jp

清水　尚憲
ジー・オー・ピー株式会社安全・安心技術研究センター所長。長岡技術科学大学大学院経営研究科システム安全専攻修了。独立行政法人労働者健康安全機構労働安全衛生総合研究所建設安全研究グループ部長を経て現職。日本機械学会フェロー。博士（工学）。
E-mail: shimizu.shoken@gop.co.jp

木村　哲也
長岡技術科学大学システム安全専攻教授。1995 年東京工業大学博士後期課程単位認定退学。長岡技術科学大学准教授等を経て 2022 年より現職。国際安全規格に基づくロボット・ドローンの実用化研究に従事。博士（工学）。
E-mail: kimura@mech.nagaokaut.ac.jp

データ駆動型制御による固定翼 UAV の姿勢制御器自動チューニングに関する研究

稲垣陽介，畠中和明，廣田光智
室蘭工業大学大学院

有人地帯での目視外飛行が可能となる新制度が開始されたことに伴い，災害発生地域などでの広範囲・長時間に及ぶ観測用途には長距離飛行が可能な固定翼 UAV の活用が望まれている．そこで，著者らの研究グループでは目標巡航速度を 60［m/s］として，オープンソースの ArduPilot を用いたフライトコントロールシステムの構築を進めている．安定した自動飛行のためには姿勢制御器の適切なチューニングが重要であるが ArduPilot に標準搭載されているチューニング支援機能は操縦者へ要求する技量が高く，高速飛行する機体での実行が困難である．そこで，データ駆動型制御の一種である VRFT（Virtual Reference Feedback Tuning）を用いた新規チューニングプロセスを構築，検証したので本稿ではその結果を報告する．

Keywords: 固定翼無人航空機，ArduPilot，データ駆動型制御，VRFT

Automatic Tuning of Attitude Controllers for Fixed-Wing UAVs Using Data-Driven Control

Yosuke Inagaki，Kazuaki Hatanaka，Mitsutomo Hirota
Graduate School of Muroran Institute of Technology

With the introduction of a new regulatory framework enabling beyond-visual-line-of-sight (BVLOS) flights over populated areas, fixed-wing UAVs capable of long-distance flight are increasingly required for extended, wide-area observation missions, such as in disaster zones. Consequently, our research group is developing a flight control system based on the open-source software ArduPilot, targeting a cruising speed of 60 m/s. Proper tuning of the attitude controller is crucial for stable autonomous flight. However, the standard tuning assistance features in ArduPilot require a high level of operator skill and are difficult to execute during high-speed flight. To address this issue, we developed and verified a new tuning process using Virtual Reference Feedback Tuning (VRFT), a data-driven control approach. This paper reports on the results of that process.

Keywords: Fixed-wing UAV, ArduPilot, Data-Driven Control, VRFT

1. Introduction

In Japan, a new regulatory framework for unmanned aircraft systems (UAVs) enabling Level 4 flights–unmanned beyond visual line of sight (BVLOS) operations in populated areas–was enacted in December 2022. This development has accelerated the expansion of UAV applications. While VTOL rotorcraft are commonly used in UAV applications, numerous scenarios require fixed-wing UAVs capable of high-speed, long-distance flight. These include surveying disaster-stricken areas affected by earthquakes,

volcanic activity, or forest fires, which are often extensive and require prolonged observation [1]. Our research group is applying fluid-dynamic thrust vectoring (FTV) technology to fixed-wing UAVs. We are advancing research aimed at achieving even higher fuel efficiency through reduced drag by decreasing tail area [2]. This is expected to broaden the scope of fixed-wing UAV applications.

Considering these circumstances, we set the target cruise speed of small fixed-wing UAVs to a relatively high range of 60–70 [m/s]. We are investigating a flight control system that enables safe autonomous operation at this speed. This study focuses on ArduPilot [3], which is being developed as open-source software.

ArduPilot incorporates three types of controllers designed to enable stable autonomous flight for a wide variety of fixed-wing UAVs. However, these controllers require appropriate tuning to match the characteristics of the specific aircraft. Tuning is typically performed by flying the aircraft and repeatedly executing specific attitude changes. However, these maneuvers were originally designed for model aircraft flying at low speeds of around 20–30 [m/s]. Completing the tuning process at the high speeds targeted in this research is expected to be difficult.

This study focuses on the attitude PID controller, one of the controllers included in ArduPilot. The first objective of this study is to identify the challenges in tuning this controller for high-speed fixed-wing UAVs. The second is to propose a new tuning process using VRFT (Virtual Reference Feedback Tuning) [4] to solve these problems. This paper reports the results of verifying the usefulness of the proposed method through simulations using an engine-propeller aircraft with a cruise speed of approximately 25 [m/s].

2. ArduPilot

ArduPilot primarily achieves autonomous flight using the three controllers shown in **Fig.1**. Specifically, these are: ① the L1 controller [5], which calculates the target roll angle to follow the target path; ② the TECS (Total Energy Control System) [6], which calculates the pitch attitude angle and throttle to achieve the target altitude and target speed; and ③ the attitude PID controller [7], which realizes the attitude calculated by the above controllers. To achieve stable flight, the PID controller must be properly tuned to the aircraft dynamics.

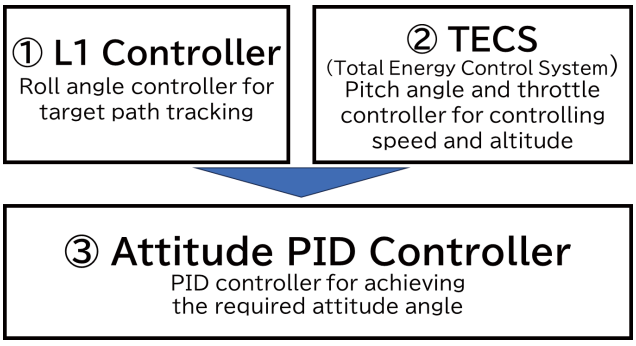

Fig.1 Overview of ArduPilot.

3. Attitude PID Controller [7][8]

Fig.2 shows a schematic diagram of the attitude PID controller.

The attitude PID controller is a cascade loop that obtains two feedback signals: the measured attitude angle and the measured attitude angular velocity. The primary control targets are the roll and pitch angular velocities, with a target range of ±90 [deg/s] in this study.

Equations (1) through (14) show the structure of the roll angle controller primarily examined in this

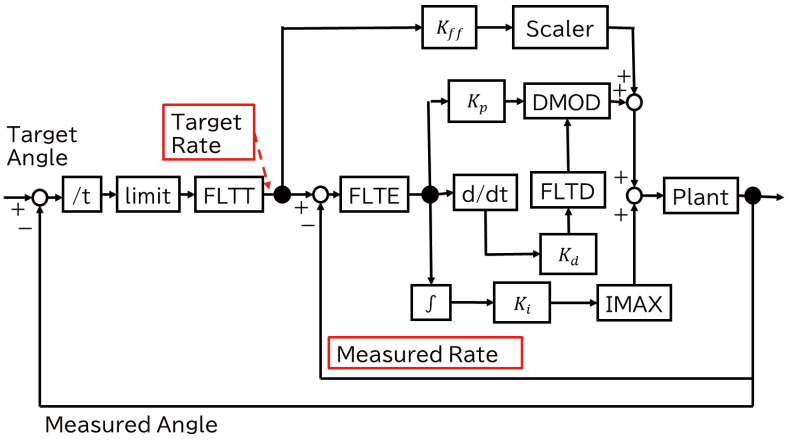

Fig.2 Overview of attitude PID controller.

paper. The difference between the target roll angle calculated by the L1 controller and the measured roll angle is obtained and differentiated to calculate the target angular velocity *target* [deg/s]. To prevent the target angular velocity from becoming excessive, it is filtered using a low-pass filter FLTT with cutoff frequency f_T [Hz], based on the difference with the target angular velocity $target_{last}$[deg/s] input to the previous controller. Here, *dt* [s] is the time interval for controller processing, and $target_1$[deg/s] is the final demand angular velocity input to the feedforward controller.

$$FLTT = \frac{dt}{dt + \frac{1}{2\pi f_T}} \tag{1}$$

$$target_1 \mathrel{+}= FLTT \cdot (target - target_{last}) \tag{2}$$

In the feedforward controller, scaling is applied to correct for differences in aircraft response to control surface input when there is a discrepancy between the set cruise speed and the actual airspeed. Furthermore, since the airspeed obtained from sensors is equivalent airspeed (EAS), it is converted to true airspeed (TAS) before calculation. This conversion variable is denoted as *EAS2TAS* in this paper. Here, *press* [Pa] is the barometric pressure during flight, $temp_g$ [℃] is the surface temperature, and *tempK* [K] is the air temperature at the flight altitude. The standard atmospheric density at sea level is 1.225 [kg/m^3], the gas constant is 287.26 [J/(kg K)], and the temperature lapse rate is 0.0065 [K/m].

$$tempK = temp_g - 0.0065 \times Alt \tag{3}$$

$$EAS2TAS = \sqrt{\frac{1.225 \times 287.26 \times tempK}{press}} \tag{4}$$

Using equations (2) and (4), the feedforward output FF_{out} is given by equation (5). Here, K_{ff} is the feedforward gain, V_{cruise} [m/s] is the setpoint cruise speed, and V_a [m/s] is the airspeed.

$$FF_{out} = K_{ff} \cdot target_1 \cdot \frac{V_{cruise}}{EAS2TAS \cdot V_a} \tag{5}$$

The angular velocity difference error between the desired angular velocity $target_1$ and the measured angular velocity is input to the feedback controller through a low-pass filter FLTE with cutoff frequency f_E [Hz]. Here, $error_{last}$ is the angular velocity difference input to the controller in the previous step, and $error_1$ is the angular velocity difference ultimately input to the controller.

$$FLTE = \frac{dt}{dt + \frac{1}{2\pi f_E}} \tag{6}$$

$$error_1 \mathrel{+}= FLTE \cdot (error - error_{last}) \tag{7}$$

In the proportional controller, the control output is calculated as in Equation (8). Here, K_p is the proportional gain, and P_{out} is the control output of the proportional controller.

$$P_{out} = K_p \cdot error_1 \tag{8}$$

In the integral controller, the control output is calculated as shown in Equations (9) and (10). However, to prevent the output from becoming excessive due to the accumulation of error, clipping is applied within an arbitrarily configurable range ($-K_{IMAX}$~K_{IMAX}). The function used for this is defined as IMAX. Within this function, if the given control output Integrator is greater than K_{IMAX}, it is clipped to K_{IMAX}; if it is less than $-K_{IMAX}$, it is clipped to $-K_{IMAX}$. Here, Integrator is the pre-processed provisional integral control output, K_i is the integral gain, K_{IMAX} is the maximum value of the integral output, and I_{out} is the integral control output.

$$Integrator \mathrel{+}= (K_i \cdot error_1) \cdot dt \tag{9}$$

$$I_{out} = IMAX(integrator, -K_{IMAX}, K_{IMAX}) \tag{10}$$

In the derivative controller, the control output is calculated as shown in Equations (11) to (14). The derivative output is filtered by a low-pass filter FLTD with cutoff frequency f_D [Hz] to prevent excessive output due to sudden target value changes. Here, derivative is the angular velocity derivative, $derivative_1$ is the filtered derivative, K_d is the derivative gain, and D_{out} is the derivative control output.

$$derivative = \frac{error_1 - error_{last}}{dt} \tag{11}$$

$$FLTD = \frac{dt}{dt + \frac{1}{2\pi f_D}} \tag{12}$$

$$derivative_1 \mathrel{+}= FLTD \cdot (derivative - derivative_1) \tag{13}$$

$$D_{out} = K_d \cdot derivative_1 \tag{14}$$

When the sum of the proportional output and derivative output (SRATE) exceeds a preset value (SMAX) that can be arbitrarily configured, scaling as shown in Equation (15) is applied. Here, M_{gain} is set to 1.5.

$$mod = SMAX/\big(SMAX + Mgain \times (SRATE - SMAX)\big) \tag{15}$$

$$P_{out} \times= mod \tag{16}$$

$$D_{out} \times= mod \tag{17}$$

Each control gain is set by default as shown in Table 1. These values are configured to achieve stable attitude control for a wide range of small fixed-wing aircraft. However, to obtain more appropriate attitude control performance, tuning tailored to the aircraft's characteristics is necessary.During the tuning process of the PID Controller for attitude control, it is primarily necessary to modify the control gains K_{ff}, K_p, K_i, and K_d mentioned Table 1.

Table 1 Default control gains.

Default K_p value	0.08
Default K_i value	0.15
Default K_d value	0
Default K_{ff} value	0.345

However, finding the optimal values by manually adjusting them while flying the aircraft automatically is nontrivial.

4. AutoTune [9]

ArduPilot includes a standard AutoTune feature to assist in tuning PID gains for attitude control. When running AutoTune, the pilot must repeatedly perform maneuvers that involve flying the aircraft in straight flight while abruptly changing its attitude. During this process, the aircraft operates in AutoTune mode (which behaves similarly to Fly By Wire A mode), where stick inputs from the RC transmitter control target attitude angles rather than control surface deflections. For example, moving the roll stick fully left or right causes ArduPilot to attempt to achieve a predefined maximum roll angle and target roll rate. During AutoTune, this action is repeated while internally varying the PID gains to find the PID settings that achieve the target roll rate. This process is similar to the limit sensitivity method proposed by J.G. Ziegler and N.B. Nichols [10], enabling proper tuning even when the dynamics of the controlled system are unknown. Fig.3 shows this process in action. The horizontal axis represents time [s]. The vertical axis of the upper graph shows roll angle, while the vertical axis of the lower graph shows roll angular velocity. The blue line indicates the target roll angle, the red line the achieved roll angle, the pink dotted line the target angular velocity, and the green line the achieved angular velocity. The period from 17 [s] to 24 [s] represents the turning segment. Fig.3 shows that the roll angular velocity gradually stabilizes toward the target value of 90 [deg/s].

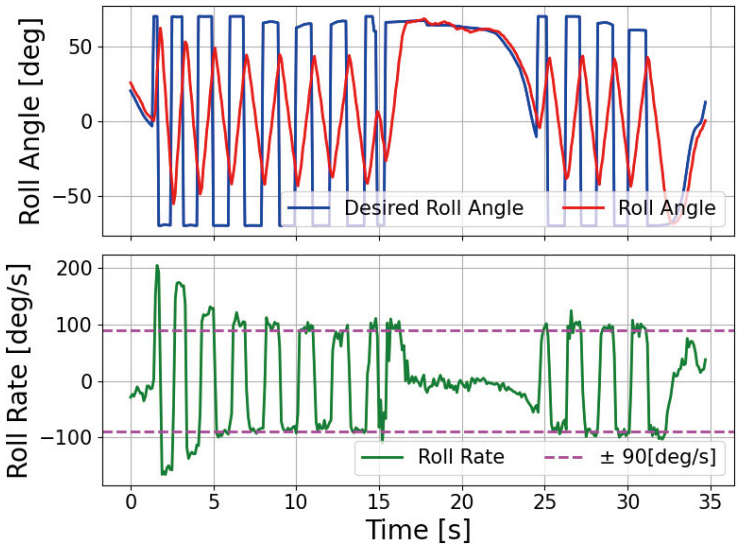

Fig.3 Action of AutoTune.

While abrupt attitude changes need not be performed continuously, dozens of such changes are required. To complete tuning for both roll and pitch within the limited flight time, it is desirable to perform multiple consecutive abrupt attitude changes during straight flight segments.

However, for the high-speed aircraft envisioned by the authors, performing this maneuver within the visual range is difficult. Assuming a cruise speed of 60 [m/s] and a visually observable straight-line distance of 400 [m], the visual range around the pilot is approximately 800 [m]. Considering that the turn must be completed within this range, the distance available for stable straight-line flight is limited to approximately 500 [m], allowing less than 10 [s] per pass for tuning. Therefore, when executing the AutoTune function on a high-speed aircraft, the pilot must perform multiple consecutive abrupt attitude changes across several round-trip straight flight segments while ensuring the aircraft remains within the visual range. This places a significant burden on the pilot, and the tuning maneuver itself increase the risk of a crash. In our previous work [11], we developed a Lua script [12] to automate the stick inputs required for AutoTune. This script enables the aircraft to perform continuous attitude changes while maintaining a straight flight path, significantly reducing the pilot's workload and the risk of losing sight of the aircraft. However, even with this automation, the fundamental issue of the long flight distance and time required to complete the tuning process remains unresolved.

5. Virtual Reference Feedback Tuning (VRFT)

To address the above issues, we propose a novel tuning process utilizing VRFT, a type of data-driven control. Data-driven control is a method that performs tuning using only a set of input-output data, treating the controlled object as a black box, without requiring iterative experiments like the limit sensitivity method. By newly constructing a process using this method, a significant reduction in required time is expected. In tuning via data-driven control, we consider two systems: the actual system with control gain ρ and the ideal system with ideal characteristics. Here, as shown in **Fig.4**, let the initial input data obtained from preliminary experiments be u_0 and the initial output data be y_0.

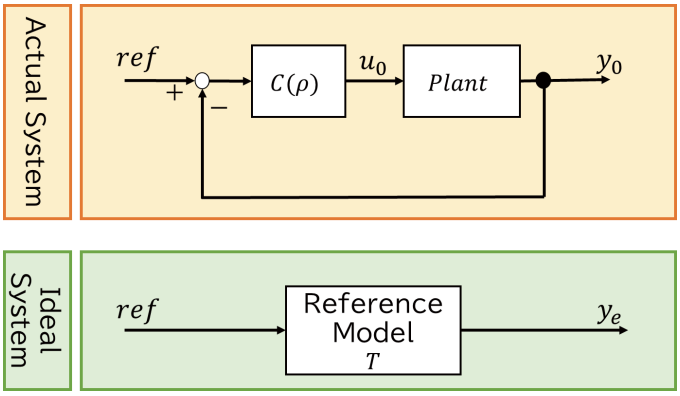

Fig.4 Actual and ideal systems.

Here, the target value ref is identical for both systems. The goal is to match the actual system's characteristics to the ideal system by modifying the control gain. The reference model exhibiting the ideal response can be arbitrarily chosen. In this study, we use the transfer function of a second-order lag system with variables ω_n (natural frequency) and ζ (damping coefficient), as shown in equation (18).

$$T = \frac{\omega_n^2}{s^2 + 2\zeta\omega_n s + \omega_n^2} \tag{18}$$

In VRFT tuning, the two systems are connected as shown in **Fig.5**. Inputting the initial data y_0 into the inverse transfer function T^{-1} of the reference model generates a pseudo-input value $T^{-1}\ y_0$ for the reference model T to output y_0. Inputting $T^{-1}\ y_0$ into the actual system yields a pseudo-reference signal r_e as shown in equation (19).

$$r_e = T^{-1}y_0 - y_0 \tag{19}$$

This pseudo-reference signal is input to the controller C(ρ) to obtain the pseudo-control output u_1.

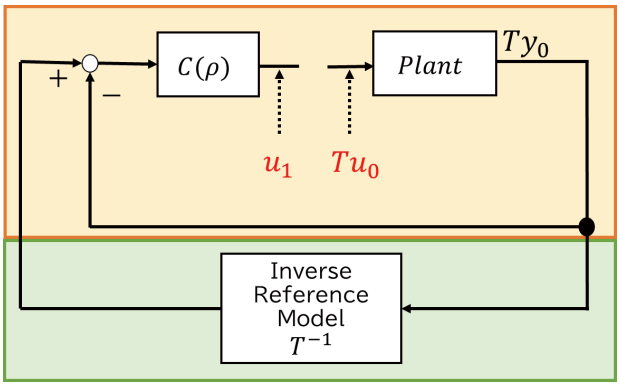

Fig.5 Block diagram of VRFT.

Since it is known from the initial experiment that the controlled system responds with y_0 to the control output u_0, tuning is complete when u_1 is made to approach u_0, ensuring input-output matching for both the reference model and the actual response. That is, tuning via VRFT reduces to an optimization problem that minimizes the following evaluation function $J_v(\rho)$ with control gain ρ as a variable.

$$J_v(\rho) = \| u_0 - C(\rho)(T^{-1}y_0 - y_0) \|^2 \tag{20}$$

Strictly speaking, to avoid the improper calculation $T^{-1}y_0$ that occurs during VRFT computation, a prefilter is applied to the initial data u_0 and y_0. Regarding prefilter design, it is generally recommended to use the reference model T directly. Applying the prefilter to equation (20) ultimately yields an evaluation function like equation (21).

$$J_v(\rho) = \| Tu_0 - C(\rho)(y_0 - Ty_0) \|^2 \tag{21}$$

This study employs a randomized search method based on Monte Carlo simulation [13] to minimize the evaluation function. Monte Carlo simulation is a method where, for a given mathematical expression, multiple values within the variable's domain are randomly generated, each calculation is performed, and the results are processed to obtain an estimated value. The flowchart is shown in **Fig.6**.

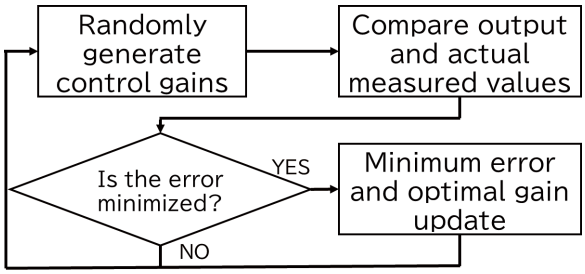

Fig.6 Flowchart of Monte Carlo Simulation.

In this study, tuning is performed by assigning a domain to each control gain and obtaining the output of a controller that replicates ArduPilot. Using this method allows for relatively easy approximation of solutions, even when the evaluation function includes complex equations like those in ArduPilot's attitude controller.

6. VRFT for two-degree of freedom control system

As explained in the previous chapter, VRFT is designed for use in single-degree-of-freedom control systems. However, as described in Chapter 3, the ArduPilot attitude controller is a two-degree-of-freedom system. While data-driven control also includes the Estimated Response Iterative Tuning (ERIT) [14] method for tuning feedforward controllers, this approach requires fixing the gain of the feedback portion. Consequently, it necessitates a two-step tuning process, increasing the total time required. Therefore, this study proposes a method to tune both controllers simultaneously by extending the VRFT theory to a two-degree-of-freedom system. This approach aims to reduce tuning time and simplify the process. A schematic diagram of VRFT extended to a two-degree-of-freedom system is shown in **Fig.7**. Here, C_{PID} denotes the PID controller and C_{FF} denotes the feedforward controller.

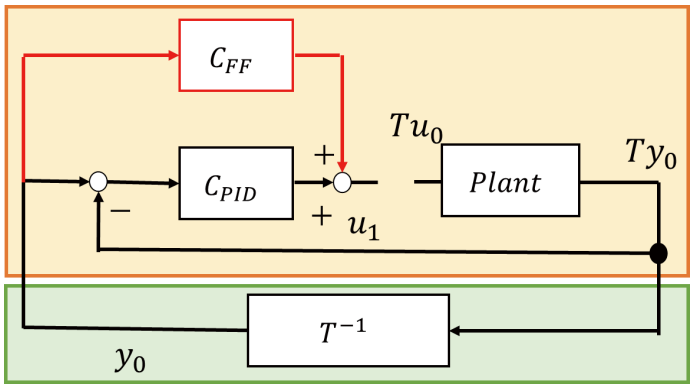

Fig.7 VRFT in Two-Degree-Freedom Control System.

In this case, the objective function takes the form given by Equation (22).

$$J_v(\rho) = \| u_0 - C_{PID}(T^{-1}y_0 - y_0) - C_{FF}(T^{-1}y_0) \|^2 \tag{22}$$

Furthermore, similar to VRFT for single-degree-of-freedom systems, applying a prefilter to the initial data u_0, y_0 ultimately yields an objective function of the form given by Equation (23).

$$J_v(\rho) = \| Tu_0 - C_{PID}(y_0 - Ty_0) - C_{FF}y_0 \|^2 \tag{23}$$

7. SITL (Software In The Loop) [15]

In this study, rather than deploying the developed process directly onto the actual hardware from the outset, we perform simulations in an SITL (Software In The Loop) environment. After conducting preliminary verification, we then proceed with experiments on the actual hardware. SITL is an environment standardly integrated into ArduPilot, and its schematic is shown in **Fig.8**. In SITL simulations, the flight controller and ground station can use the exact same firmware and parameters as in actual flight tests. The information exchanged between the flight simulator and the hardware is identical to that in actual flight tests. Therefore, if the aircraft is appropriately modeled in the simulator, results obtained from SITL simulations are expected to closely resemble those from actual flight tests.

8. Method

8.1 Aircraft specifications and SITL overview

This research uses relatively low-speed aircraft for functional verification. After confirming its usefulness, we will consider installing it on higher-speed aircraft in future work. The test aircraft is the Kyosho Calmato α-40 SPORTS (Wingspan 1400 [mm], Weight 3.19 [kg], 2-stroke 0.40 in³ engine). The

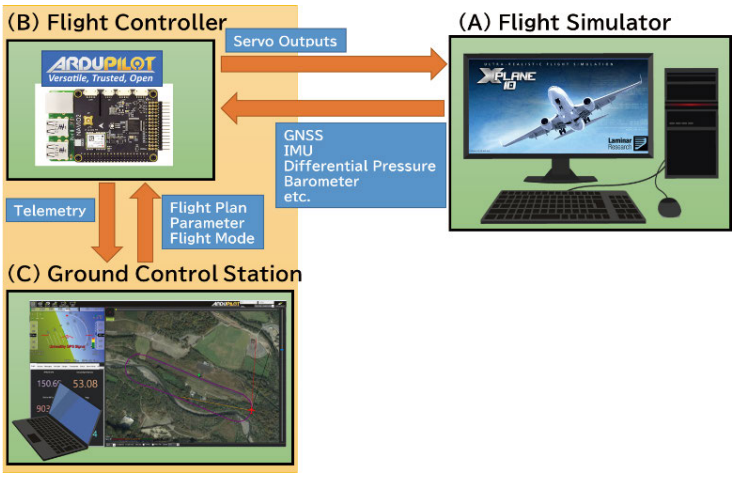

Fig.8 Overview of SITL.

flight simulator constituting the SITL utilized X-Plane 10. Flight simulations were conducted using a model equivalent to the test aircraft [16]. Figure 9 shows the test aircraft model created within the flight simulator.

Fig.9 Calmato in SITL.

Additionally, the flight test site, Shiraoi Gliding Field, was recreated using the included World Editor. GNSS position data was also integrated to establish a simulation environment matching the actual flight test. This enables sharing the target flight path between simulation and actual flight tests, allowing flights verified in simulation to be directly executed in the actual flight test.

8.2 Design of the reference model

In VRFT tuning, it is crucial that the reference model is appropriately designed. Therefore, the variables of the reference model are determined using Monte Carlo simulations based on angular velocity input-output data obtained from prior research, which achieved angular velocities of ±90 [deg/s]. Equation (18), representing the reference model used in this study, is shown again.

$$T = \frac{\omega_n^2}{s^2 + 2\zeta\omega_n s + \omega_n^2} \tag{18}$$

As seen in Equation (18), the reference model has two variables. We assign ranges to these two variables, generate 1000 random values for each, and find the pair of variables that minimizes the sum of squared errors between the output angular velocity when the desired angular velocity is input to the reference model and the actual measured angular velocity in the experiment. The ranges for each variable are as shown in Table 2.

Table 2 Range of variables in the reference model.

ω_n	0.01～50 [rad/s]
ζ	0.01～2.0

8.3 New process evaluation using VRFT

Simulations were performed using SITL with the default attitude control PID gains installed. Data involving angular velocity changes was acquired by executing an automatic circular flight. The main simulation conditions are shown in Table 3. The cutoff frequencies for the filters (f_T, f_E, f_D) were determined based on the results of a preliminary flight test using the AutoTune function on the actual aircraft. The specific values obtained from the flight log were rounded to the nearest integer for simplicity in the SITL simulation.

Table 3 Flight conditions.

Proportional Gain	0.08
Integral Gain	0.15
Derivative Gain	0
Feedforward Gain	0.345
Roll Rate Max	90[*deg/s*]
Integral Output Max	10[*deg/s*]
Cruise Speed	25[*m/s*]
f_T	5[*Hz*]
f_E	0[*Hz*]
f_D	10[*Hz*]

The aircraft is given a rectangular target path using the WayPoint navigation function standard on ArduPilot. WayPoints have two parameters: coordinates and a radius at which the aircraft is considered to have arrived. The aircraft flies along the target path, which is a straight line connecting each WayPoint, as shown in Fig.10.

After the simulation completes, review the log data, select the turning section where angular velocity response occurs, and extract the necessary data. The data to extract is as shown in Table 4. Input each data point into the ArduPilot-replicated controller, obtain the controller output, and calculate the sum of squared errors compared to the experimental values. Repeat this calculation 5000 times within the control gain's defined range. The combination yielding the smallest sum of squared errors is adopted as

Fig.10 Flight plan.

the tuned gain. The defined ranges for each gain are as shown in **Table 5**. Perform SITL again with the attitude control PID gains obtained via VRFT installed, and confirm that the target attitude angular velocity (±90 [deg/s]) is achieved.

Table 4 Required data.

time	Time[s]
ref	Target Rate [deg/s]
y_0	Measured Rate [deg/s]
FF_0	Feedforward Output
P_0	Proportional Output
I_0	Integral Output
D_0	Derivative Output
press	Pressure [Pa]
alt	Altitude [m]
V_a	Airspeed [m/s]
$temp_g$	Ground Temperature[℃]

Table 5 Range of control gains.

Feedforward Gain	0.0～0.5
Proportional Gain	0.01～0.1
Integral Gain	0.01～0.1
Derivative Gain	0.0001～0.01

9. Results

First, it should be noted that the horizontal axis of all graphs shown in this section represents the elapsed time from the start of the evaluation section [s].

Fig.11 shows a graph comparing the reference model's angular velocity response with the experimentally obtained angular velocity response. The blue line represents the target angular velocity, the green dotted line shows the experimentally obtained angular velocity response, and the red line indicates the reference model's response. Furthermore, the final reference model variables were determined as shown in **Table 6**.

Fig.12 through 15 show the outputs from each controller obtained via SITL simulation and VRFT tuning. In each graph, the vertical axis represents the control output [deg/s]. The blue line indicates the control output obtained experimentally, while the red line shows the control output calculated via VRFT tuning. The closer these two lines align, the better the tuning result is considered.

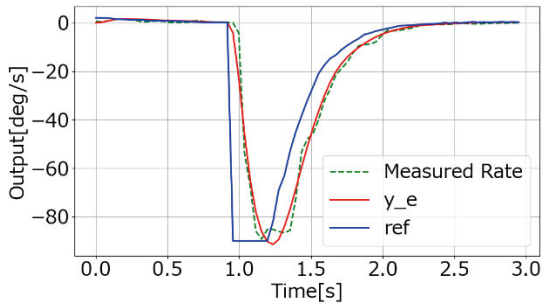

Fig.11 Comparison of angular velocity responses.

Table 6 Reference model variables.

ω_n	15.02 [rad/s]
ζ	0.7673

The feedforward outputs are largely consistent before and after tuning, but the other outputs do not match. Regarding the derivative output, since the default gain is 0, this error is considered inevitable when tuning from the default settings. For the proportional output, the discrepancy is thought to arise from the responsiveness of y_0 to the target angular velocity ref in the simulation. **Fig.16** shows the blue line as the target angular velocity ref [deg/s], the red line as the measured angular velocity y_0 [deg/s],

the orange line as Ty_0 [deg/s], the green line as the control input in VRFT, i.e., the pseudo-reference signal r_e ($=y_0-Ty_0$) [deg/s], and the purple line shows the angular velocity difference $error_{SITL}$ input to the controller in the simulation.

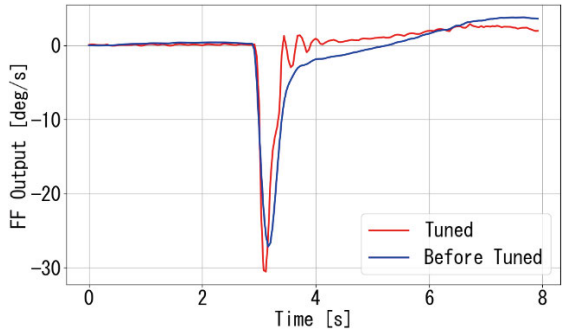

Fig.12 Comparison of feedforward outputs.

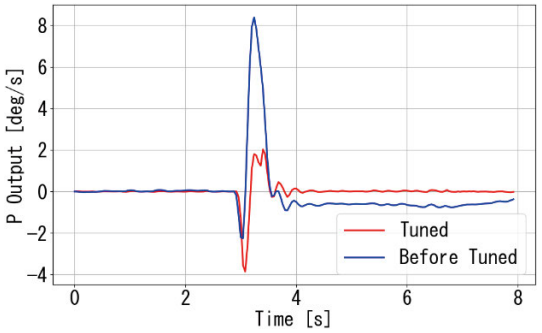

Fig.13 Comparison of proportional outputs.

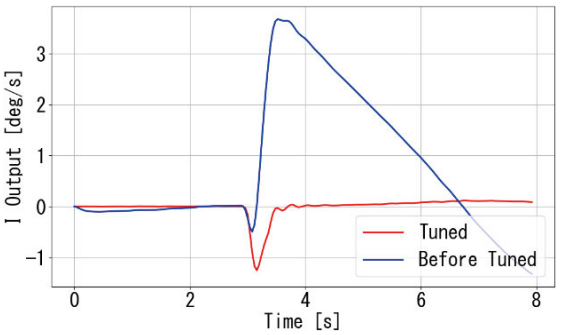

Fig.14 Comparison of integral outputs.

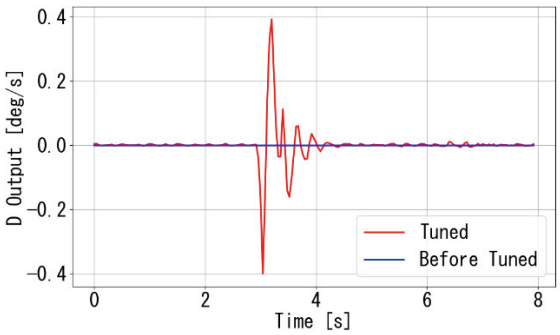

Fig.15 Comparison of derivative outputs.

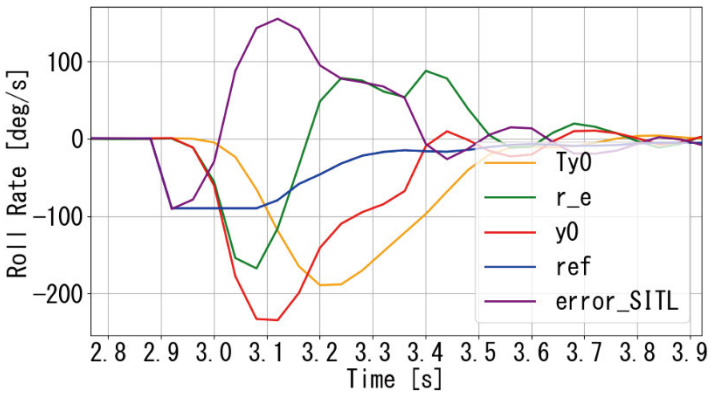

Fig.16 Reference and measured roll rate.

From Fig.16, the reference angular velocity ref in the simulation changes abruptly at the start of the turn and gradually approaches zero towards the end of the turn. However, y_0 does not exhibit such abrupt changes as ref. Comparing $error_{SITL}$ and r_e, the time from when the error begins to be detected until the error reaches its maximum is approximately 0.1 [s] later for r_e. Conversely, both gradually change towards the end of the turn. Consequently, even with the same gain, the tracking performance of the control output obtained in the simulation changes between the turn initiation phase and the subsequent phase. The Monte Carlo simulation used in this study is fundamentally a method for obtaining approximate solutions. Therefore, it is considered that the error arises because the simulation

cannot fully account for the difference in tracking performance between the first and second halves. Additionally, the default gain being too large relative to the target angular velocity may have caused excessive control output, preventing full rise and thus poor tracking. Regarding the integral output, since this tuning only extracts a portion of the turn, error likely arises because elements that would normally be accumulated from the start of flight are not considered.

Table 7 shows the default gains, gains obtained via AutoTune, and gains after tuning using VRFT.

Table 7 Comparison of gains.

	K_p	K_i	K_d	K_{ff}
Default	0.08	0.15	0	0.345
AutoTune	0.052	0.052	0.0027	0.130
VRFT	0.023	0.058	0.0002	0.140

Table 7 shows that the control gains obtained via VRFT are significantly smaller than those obtained via AutoTune, except for the feedforward gain and integral gain. This is likely due to the controller developed here not fully replicating the intricate internal structure of ArduPilot, and the fact that values calculated via Monte Carlo simulation are only approximate solutions. Furthermore, even using a PC, the Monte Carlo simulation calculations took about 10 seconds, meaning that when installed on the actual aircraft, it could impose a load on the flight controller and potentially affect the accuracy of the autopilot.

Fig.17 shows the simulation results with the tuned gains installed. The vertical axis represents roll angular velocity [deg/s]. The blue line indicates the target angular velocity, the yellow-green line shows the roll angular velocity response with the default gains installed, the green line shows the response with the AutoTune-derived gains installed, and the red line shows the response with the VRFT-derived gains installed.

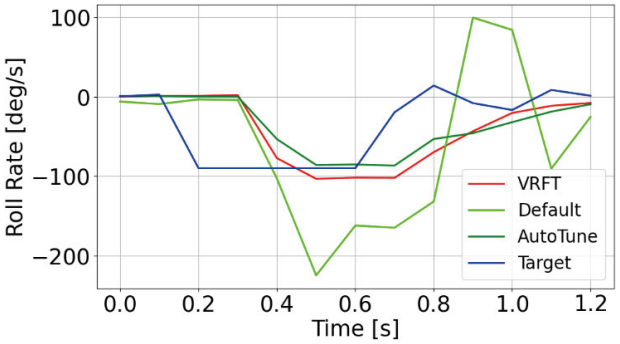

Fig.17 Comparison of roll rate.

As seen in Fig.17, while the maximum value of the red line is slightly larger than the target roll rate of ±90 [deg/s], the fact that this state can be tuned to from the default state with a single attitude change demonstrates the usefulness of this method.

Results from performing VRFT tuning again using data obtained with the gains from VRFT are shown in Fig.18 through 21. The information represented by the horizontal and vertical axes and the lines is the same as in Fig.12 through 15. In the second tuning, unlike the first, all outputs except the integral output generally follow the target. This is likely because the initial tuning reduced the magnitude of each control output, allowing them to keep up with the target. However, poor tracking due to differences in the rate of change of the error quantity is evident, indicating further improvement is needed.

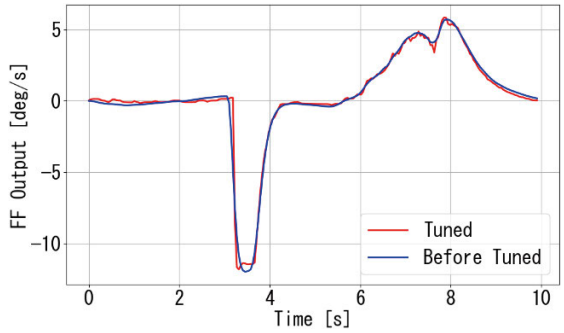

Fig.18　Comparison of feedforward outputs (2).

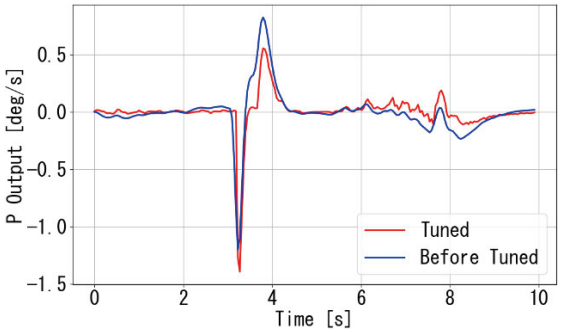

Fig.19　Comparison of proportional outputs (2).

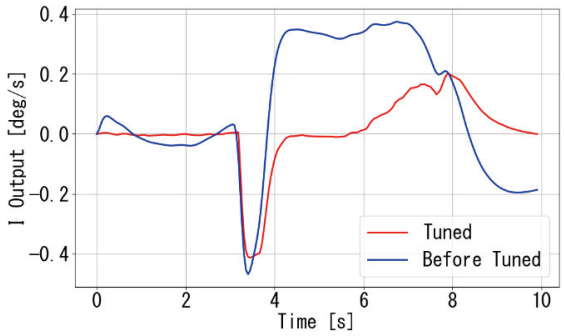

Fig.20　Comparison of integral outputs (2).

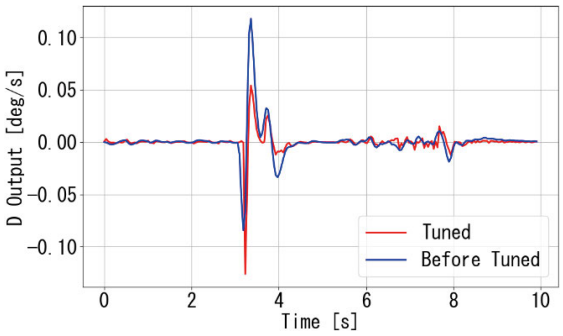

Fig.21　Comparison of derivative outputs (2).

The results of the second tuning are shown in Table 8 and Fig.22. In Fig.22, the orange line represents the roll angular velocity when using the gains obtained from the second VRFT.

Table 8　Comparison of gains (2).

	K_p	K_i	K_d	K_{ff}
Default	0.08	0.15	0	0.345
AutoTune	0.052	0.052	0.0027	0.130
VRFT (1)	0.023	0.058	0.0002	0.140
VRFT (2)	0.017	0.038	0.0001	0.119

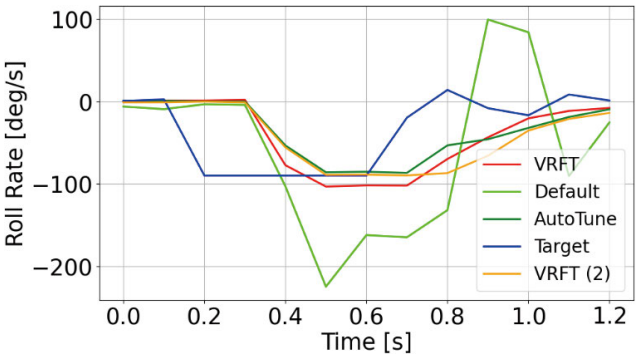

Fig.22　Comparison of roll rate.

The results above show that during the second tuning, a gradual but noticeable tracking of the target angular velocity was observed. Additionally, the minimum angular velocity appears to be approximately −90 [deg/s]. This indicates that tuning is completed after two turns. However, compared to the angular

velocity response when using gains obtained from AutoTune, the tracking performance relative to the target angular velocity is poor, indicating a need for improvement.

10. Conclusion

This study aimed to resolve issues concerning the tuning of the attitude PID controller when adopting ArduPilot as the flight controller for a high-speed small fixed-wing UAV. We proposed a novel tuning process using VRFT and verified its effectiveness through simulations using an engine-propeller aircraft. This method was shown to be highly useful, as it significantly reduces the pilot's burden during tuning of high-speed aircraft, eliminating the need for continuous abrupt attitude changes required by conventional methods. Furthermore, since tuning can be completed in just two turns starting from the default control gains, it suggests a substantial simplification of the tuning process compared to ArduPilot's standard AutoTune feature. However, challenges remain, including the lack of theoretical justification for extending VRFT to two-degree-of-freedom systems, the requirement of several tens of seconds to compute the Monte Carlo simulations themselves, and the need for improvement in the data used during the tuning of the integral elements.

Received：January 30, 2026
Accepted：March 16, 2026

References

[1] Martínez-de-Dios, et. al., "Automatic Forest-Fire Measuring Using Ground Stations and Unmanned Aerial Systems" Sensors, 11, 2011, pp. 6328–6353.
[2] Mitsutomo Hirota, Kazuaki Hatanaka, Tsutomu Saito, Srisha M. V. RAO, "Characteristics of Subsonic FTV Nozzle and Its Flight Demonstration", The Japan Society for Aeronautical and Space Science's collection of papers, 2018, 66(1), pp. 1–6. [Translated from Japanese]
[3] ArduPilot Development Team. ArduPilot Plane, Available online: https://ardupilot.org/plane/index.html, accessed on 16 January 2026.
[4] Campi, M. C., Lecchini, A., & Savaresi, S. M., Virtual reference feedback tuning: a direct method for the design of feedback controllers. Automatica, 38(8), 2002, pp. 1337–1346.
[5] S. Park, et. al., "A new nonlinear guidance logic for trajectory tracking", AIAA Guidance, Navigation, and Control Conference and Exhibit, 2004, pp. 16–19.
[6] P. Jimenez, et al., "Experimental validation of total energy control system for UAVs", Energies 2020, 13(1), 14.
[7] S. Baldi, et al., "ArduPilot-Based Adaptive Autopilot: Architecture and Software-in-the-Loop Experiments", IEEE Transactions on Aerospace and Electronic Systems, 58(5), 2022, pp. 4473–4485.
[8] ArduPilot Development Team. Roll, Pitch, and Yaw Controller Tuning, Available online: https://ardupilot.org/plane/docs/new-roll-and-pitch-tuning.html, accessed on 16 January 2026.
[9] ArduPilot Development Team. Automatic Tuning with AUTOTUNE, Available online: https://ardupilot.org/plane/docs/automatic-tuning-with-autotune.html, accessed on 16 January 2026.
[10] J. G. Ziegler, N. B. Nichols, ROCHESTER, N.Y., "Optimum Settings for Automatic Controllers", Trans. ASME. Nov 1942, 64(8), 1942, pp. 759–765.
[11] Yosuke Inagaki, Nanako Suzuki, Kazuaki Hatanaka, Mitsutomo Hirota, "A Research on Automatic Tuning of the Attitude Control System of Unmanned Aerial Vehicle Flying at High Speeds in Conjunction with SITL", The 63rd Aviation Engine and Space Propulsion Symposium / Northern Branch 2024 Symposium / The 5th Reusable Space Transportation Symposium, 2024.
[12] ArduPilot Development Team. Lua Scripts, Available online: https://ardupilot.org/copter/docs/common-lua-scripts.html, accessed on 16 January 2026.
[13] Samik Raychaudhuri, "Introduction to Monte Carlo simulation", 2008 Winter Simulation Conference, 2008, pp. 91–100.
[14] Osamu Kaneko, Introduction to Data-Driven Control, Measurement and Control Selection Series 7, edited by The Society of Instrument and Control Engineers, CORONA PUBLISHING CO., LTD. (2024), pp. 207–223. [Translated

from Japanese]
[15] ArduPilot Development Team, SITL Simulator (Software in the Loop), Available online: https://ardupilot.org/dev/docs/sitl-simulator-software-in-the-loop.html, accessed on 17 January 2026.
[16] RC Calmato Alpha 40 sport UAV 1.00, Available online: https://forums.x-plane.org/files/file/21159-rc-calmato-alpha-40-sport-uav/, accessed on 17 January 2026.

Yosuke Inagaki
Born in 2001. Enrolled in the Graduate School of Muroran Institute of Technology in 2024, majoring in Aerospace Engineering.
E-mail: 24042003@muroran-it.ac.jp

Mitsutomo Hirota
Mitsutomo Hirota completed the doctoral course, without degree at Keio University's Graduate School of Science and Technology in 2001. He then became a research assistant at Tohoku University's Graduate School of Engineering in 2001, where he engaged in fundamental combustion research and laser measurement in high-speed airflow. He earned his Ph.D. (Doctor of Engineering) from the Graduate School of Science and Technology, Keio University in 2003. Subsequently, he served as Lecturer at the Faculty of Engineering, Muroran Institute of Technology in 2007, Lecturer at the Graduate School of Engineering, Muroran Institute of Technology in 2008, Visiting Researcher at the University of California, San Diego in 2012, Associate Professor at the Graduate School of Engineering, Muroran Institute of Technology in 2014, and became Professor at the Graduate School of Engineering, Muroran Institute of Technology in 2023. During this period, he also engaged in fundamental research on shock waves, combustion control research, and fire suppression strategy research.

Kazuaki Hatanaka
Kazuaki Hatanaka earned his Ph.D. in Engineering from Muroran Institute of Technology in 2013. After working in the private sector, he joined Tohoku University as an assistant professor in 2014, where he conducted research on the medical applications of shock waves. Since 2016, he has been an associate professor at Muroran Institute of Technology, engaged in aerospace engineering research.

一般社団法人 日本 UAS 産業振興協議会（JUIDA）

JUIDA は、日本の無人航空機システム（UAS）の、民生分野における積極的な利活用を推進し、UAS 関係の新たな産業・市場の創造を行うとともに、UAS の健全な発展に寄与することを目的とした中立、非営利法人として、2014 年 7 月に設立されました。

国内外の研究機関、団体、関係企業と広く連携を図り、UAS に関する最新情報を提供するとともに、さまざまな民生分野に最適な UAS を開発できるような支援を行っています。同時に、UAS が安全で、社会的に許容されうる利用を実現するために、操縦技術、機体技術、管理体制、運用ルール等の研究を行うとともに政策提言を行っています。

Technical Journal of Advanced Mobility
次世代移動体技術誌

第 7 号

発行日　：2026 年 1 月 20 日
編集・発行　：一般社団法人日本 UAS 産業振興協議会
東京都文京区本郷 5-33-10
いちご本郷ビル 4F
URL　：https://uas-japan.org/
email　：journal@uas-japan.org

ISSN　2435-5453